DEVELOPMENT OF A HIGH POWER DENSITY MOTOR

FOR AIRCRAFT PROPULSION

A Thesis

by

IMOUKHUEDE TIM ODION DIBUA

Submitted to the Office of Graduate Studies of
Texas A&M University
in partial fulfillment of the requirements for the degree of

MASTER OF SCIENCE

December 2006

Major Subject: Mechanical Engineering

DEVELOPMENT OF A HIGH POWER DENSITY MOTOR

FOR AIRCRAFT PROPULSION

A Thesis

by

IMOUKHUEDE TIM ODION DIBUA

Submitted to the Office of Graduate Studies of
Texas A&M University
in partial fulfillment of the requirements for the degree of

MASTER OF SCIENCE

Approved by:

Chair of Committee, Alan Palazzolo
Committee Members, J. N. Reddy
Vikram Kinra
Head of Department, Dennis O'Neal

December 2006

Major Subject: Mechanical Engineering

ABSTRACT

Development of a High Power Density Motor

for Aircraft Propulsion. (December 2006)

Imoukhuede Tim Odion Dibua, B.S., Texas A&M University

Chair of Advisory Committee: Dr. Alan Palazzolo

Electric propulsion has been studied for a long time. Most of the electrically propelled vehicles that have been developed however have been ground vehicles. Recent research by NASA has promoted the development of electric aircraft. Most aircraft are currently powered by heavy gas turbine engines that require fueling. The development of electric motors to replace gas turbines would be a big step towards accomplishing more efficient aircraft propulsion.

The primary objective of this research extends previous work by developing a high power density motor for aircraft propulsion. This design is novel because it does not require a dynamometer to provide the torque to drive the vehicle. Equally important for successful testing of the motor was the design and development of a spin pit interface that was used as a containment vessel during testing.

The research led to a designed, fabricated, assembled, modeled, and tested motor. Voltages, currents and power outputs of the motor were measured and used to determine the motor's efficiency. The gaps between the motor's magnets were related to the current and power it produced, and modifications were made based on this relation. The

vibrations of the motor were also studied and MATLAB codes were written and used to reduce these vibrations.

Significant among the objectives was monitoring the temperatures of the motor's stators due to their close association with the rotating parts. The windage and friction losses between the stators and the magnets provided a challenging hurdle in the research. These windage and friction losses were predicted, analyzed and measured, and modifications were made to reduce them.

Finally, results were compiled, tabulated, and analyzed. Results obtained before and after the modifications were compared, and these comparisons were used to assess the necessity and effectiveness of the modifications. The efficiency of the motor was found to be 82.9% and the power density was evaluated as 33.1 W/lb based on a rotor weight of 497 lb. It was concluded that the litz wire used in the motor has high, frequency related impedances that could be reduced but not eliminated.

DEDICATION

To my family

ACKNOWLEDGEMENTS

I would like to thank my committee chair, Dr. Alan Palazzolo, for his leadership, guidance and support throughout the course of this research, and for providing me with this paid research at a time when I really needed financial support. This research would never have been possible without his constant supervision and availability to answer questions. I would also like to thank my committee members, Dr. J.N. Reddy and Dr. Vikram Kinra, for their help and support.

Thanks also to my friends and colleagues and the Mechanical Engineering Department faculty and staff for educating me and making my time at Texas A&M a great experience. I also want to extend my gratitude to the National Aeronautics and Space Administration for funding the research.

I would also like to thank Albert F. Kascak, Ben Ebihara, and Randall Tucker for the design and initial fabrication of the rig, as well as their great ideas and direct help with numerous tests. Thanks also to Jeff Trudell and Andrew Kenny for model predictions, which were essential to the success of the research, and to Junyoung Park for his constant help and support.

Finally, thanks to my family for their moral support and encouragement, and especially to my parents for their financial support.

TABLE OF CONTENTS

Page

Page

LIST OF FIGURES

Page

Page

Page

Page

Page

LIST OF TABLES

Page

INTRODUCTION

Background

Most aircrafts use a gas turbine engine for their propulsion. Gas turbine engines require some kind of fuel such as kerosene, or jet fuel for their operation. This means that aircrafts with such engines have to be fueled after some period of operation and so cannot be used constantly for extended periods of time. The fuels required by gas turbine engines are expensive and their prices have been growing dramatically over the past few decades. Fuels are combustible and thus increase the risk of fire hazards and explosions in aircraft engines. Also, the combustion of fuels by gas turbine engines produces environmentally harmful emissions and severe atmospheric pollution. Most fuels used for gas turbine engines are products of crude oil which is by no means unlimited. Over the past century, the availability of crude oil has peaked, is starting to drop, and will soon be at ground zero. All of these facts make it necessary to find new ways for aircraft propulsion. One such way is electric propulsion, which requires an electric motor for its operation.

The National Aeronautics and Space Administration (NASA) conducts and funds research to advance the state of the art in aeronautics, including improvements in aircraft design leading to enhanced performance in areas such as noise, emissions and safety.

This thesis follows the style of the ASME Journal of Engineering for Gas Turbines and Power.

enabling technologies for an all-electric aircraft. The operation of an all-electric aircraft requires the design of more compact and efficient electrical motors. As a result, a scaled blade-tip-drive test rig has been designed.

Statement of Objective

The primary objectives of the research are to co-design, build and further advance by test

a) a prototype motor with extraordinary power-density
b) a test platform for the motor, that does not require a dynamometer to apply load to the motor.

The secondary objectives are as follows:

- develop cooling techniques to counter windage and ohmic heating
- compare test and predicted results
- optimize operation of the motor by adjusting phasing and adjusting gaps.

Statement of Contribution

a) Demonstrated the feasibility for employing an integral generator as a load source for the prototype motor thereby dispensing a requirement to install an in-line dynamometer to apply torque to the motor.
b) Demonstrated a measured power density of 33.1 W/lb based on a rotor weight of 497 lb and 8.8 W/lb based on the combined rotor and housing weight of 1870 lb.
c) Demonstrated a measured motor efficiency of 82.9%.

d) Demonstrated mechanical operation of MG at 5000 rpm with acceptable vibration levels.

e) Demonstrated closed circuit electrical operation at 5000 rpm.

f) Implemented following modifications of base design to enhance stator cooling:

- Smoothing of internal air passages
- installation of cooling air manifold to inject air into rotor/stator gaps
- drilled holes in rotor to emulate a Tesla pump

g) Provided analysis, prediction and measurement for windage related power loss.

h) Provided analysis, prediction and measurement for stator temperature.

i) Provided analysis, prediction and measurement for cooling derived from drilling holes in the rotor.

j) Provided an analysis relating gaps between stator and rotor to voltages, currents and power produced by the test rig.

k) Provided current, generated voltage and power plots vs. speed from 0-5000 rpm.

Statement of Work

(a) Perform Literature Search – A search was carried out to find literature and previous research that showed that the current research topic was indeed useful and a continuation of past research and designs.

(b) Final design drawings for test rig – Design drawings had already been carried out by the research sponsors at NASA Glenn. Some drawings were modified and the rest confirmed to prepare for the fabrication of parts.

(c) Stator Sample Test for maximum current – Since there were going to be high currents going through the wires wound in the stators, a test was carried out to see exactly how much current it would take to warp the stator material. This test was carried out by Randy Tucker.

(d) Machining of parts – Parts were fabricated, some of them machined by the student and others contracted out to machine shops around.

(e) Assembling of parts – Parts were assembled based on the final design.

(f) Preparation of Test Facility (Spin Pit) – With the weight of the entire test rig and the high speeds at which they were going to be rotating, it was necessary to design, develop and build a test facility to ensure safety during testing. A spin pit was designed and built by Randy Tucker. It was made to be independent of the building and was rigged up with a secure flange to hold the rig in the pit during testing.

(g) Low Speed Open and Closed Circuit Tests – The rig was tested at low speed both with an open circuit and a closed circuit. Open circuit tests measured open circuit voltages while closed circuit tests measured currents and closed circuit voltages, and determined the output power.

(h) High Speed Open and Closed Circuit Testing – Open and closed circuit tests were also carried out at high speed to determine the current going through the rig. These were used to determine the power output and then to evaluate the efficiency and the power density of the motor.

(i) Search for Appropriate Motor and Drive (Trial and Error) – A few motor and drives were used, in order to find the appropriate auxiliary motor. There was no way to test each one so it was basically a trial and error to figure out the most appropriate driver.

(j) Balancing Test Rig – During testing, there were vibrations due to imbalance on the rotor. A balancing formula was used to determine balance weights that were placed at various positions on the rotor.

(k) Modifications of Test Rig for Cooling of Stator – The stators had a large temperature rise as the speed of the motor was increased. This was possibly due to factors such as windage losses, eddy currents, etc. Numerous modifications were made to the rig to enhance the cooling of the stator.

(l) Final Tests – Final tests were run after all the necessary modifications were made.

(m) Conclusions – Data reduction was carried out on the final results to determine some necessary variables.

Literature Review

The idea of electric propulsion of vehicles has been around for a very long time. Different vehicle and aircraft companies have been carrying out research to create better vehicle propulsion systems. For example, General Motors' work with electric vehicles started in 1916 when GMC produced a number of electric trucks using lead-acid batteries. This research however, disappeared with the development of electric self starter for the gasoline powered vehicles. In 1960's, GM resurrected its research on electric vehicle propulsion systems due to increasing awareness of air quality. Since

then, GM has developed several electric vehicles for land transportation. Based on GM's research and developments, Rajashekara argues that motor developers will need to focus on efficiency improvement to increase the vehicle range [1]. All of GM's developments were land vehicles and nothing was really geared towards aircrafts.

Aircrafts have been in existence for a very long time. Aircrafts in the past and most today use some kind of fuel combustion system which could be very harmful to the environment. Kohout and Schmitz explained that it is necessary to find alternative power sources for aircrafts such as fuel cells "as a means to substantially reduce or eliminate environmentally harmful emissions" [2]. These alternative power sources cannot directly propel aircrafts but will have to be a power source for an electric motor.

Masson and Luongo pointed out that NASA conducts and funds research to improve aircraft design. A particular initiative involves development of an all-electric aircraft requiring significant improvement in certain technologies. Electrical aero-propulsion requires the design of more compact and efficient electrical motors. They explained that in order to increase the power density of these motors, the weight / size must be minimized and the air gap flux density must increase significantly [3].

Masson et al. addressed some design considerations to be taken into account when designing motors for aircraft propulsion. They noted that the possibility of designing high power density motors, such as the proposed model, operating at reasonable temperatures allows for new applications in mobile systems in which size and weight represent key design parameters. They stated that "electric propulsion has the potential to be the next significant leap in aircraft propulsion technology" [4].

In 1996, the solar powered vehicle “Aurora”, using as in-wheel electric motor, entered the 3010 km Darwin – Adelaide World Solar Challenge solar car race. Ramsden et al. reported that the brushless DC motor used was more efficient and lighter than all other direct-drive motors, and more efficient than all motor / gear combinations in the race. They explained their design, giving reasons for different choices and showing why they used the “Halbach magnet array” arrangement for the magnets. They presented tables showing the outstanding results of the “Aurora” motor and compared its performance to that of internal combustion engines and drive trains [5]. Their motor is a small scale brushless DC motor and was used in the wheel of the Aurora. It was only used at low speeds of about 3000 rpm. The motor being developed in this research will be used in aircraft blade tips, will not require a dynamometer to supply the load, and could go to very high speeds of about 10,000 rpm. This has not been done before.

DESIGN AND ASSEMBLY OF THE MOTOR AND SPIN PIT INTERFACE

Statement of Need

There exists the need to develop a high power density motor for aircraft propulsion. There also exists the need to design and build a safe testing facility for the high power density motor.

Design Overview

The blade tip rig was originally designed by researchers at NASA and by Randy Tucker. The rig is a scaled version of a DC brush-less motor, which would be located in the shroud of a thrust fan and connected to the fan as shown in Fig. 1. This geometry is

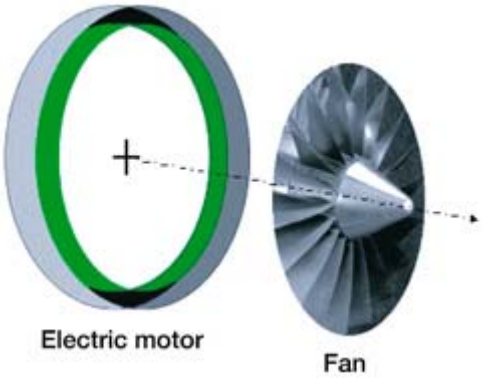

Fig. 1 Motor coupled with fan in blade tip [6]

very attractive since the allowable speed of the armature is approximately the speed of the blade tips. The magnetic pressure generated in the motor, acts over a large area; and thus, produces a large force. This large force multiplied by the large velocity results in a high power density motor.

The unique feature of this rig is that the electrical current and voltage required to drive the motor are provided by a generator. The torque required to drive the generator is provided by the test motor and an auxiliary motor. The auxiliary motor drives the test motor and generator through a pulley as is shown in Fig. 2. The test motor and generator are supported by oil mist lubricated ball bearings with a rub bearing backing up the ball

Fig. 2 Test motor coupled with auxiliary motor [6]

bearings. Later, when the rig will be used for its application, a different motor drive or other power sources such as solar panels and fuel cells will be used to drive the motor and the torque will be absorbed by the generator. The rig also has the unique feature of rotating back iron that acts as both structural support and return path for the magnetic flux.

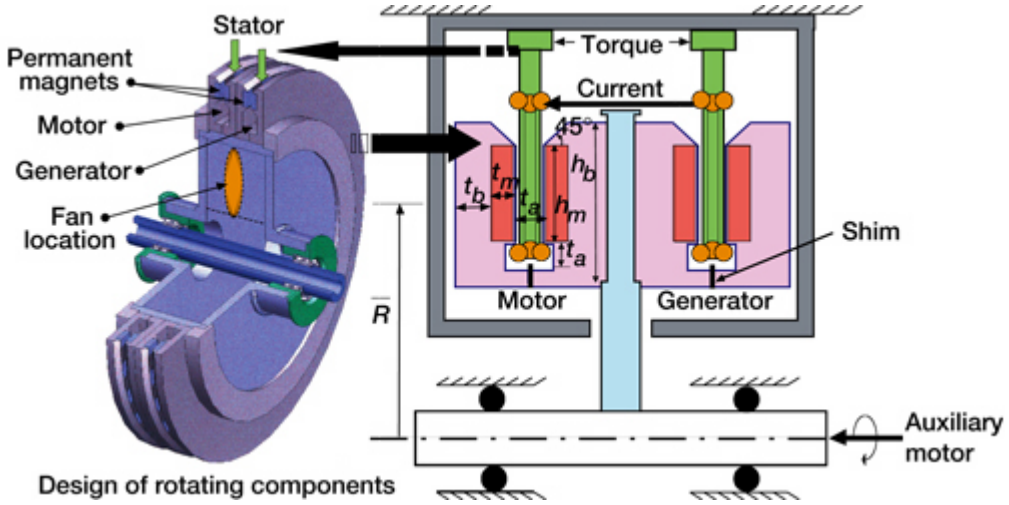

Fig. 3 Labeled drawing of design [6]

The back iron does not have to be laminated because it is rotating with the rotating field of the permanent magnets. The motor and generator are back to back and the generator can also be converted to a motor, thus doubling the power. A labeled schematic of the test rig is shown in Fig. 3.

As stated earlier, the motor is a DC brush-less motor, therefore the current must be switched every time a wire crosses a magnet edge. This is automatically accomplished because the generator is identical to the motor and they are mounted 180º out of phase. The motor back voltage is less than the generator voltage. The motor back voltage is controlled by the shim used to set the gap between the motor magnets. This gap determines the magnetic flux density between the magnets. The force on the wires in the stator is the product of this magnetic flux density, the current, and the length of the wire. The force on the stator is the sum of the forces on all the wires. The power is the product of the force and the velocity. The wires are looped radial inward and then outward on the non-conducting stator. This design puts the highest number of wires in

the highest magnet field for the longest time, and at the highest speed. The weight of the motor is the combined weight of the back iron, the magnets, and the wires and stator. The power to weight ratio is then proportional to the current in the wires and the heat transfer from the wires.

Design Requirements

The original design requirements are shown in the Table 1.

Table 1 Original design requirements

Parameter	Quantity
Power	115 KW
Voltage	576V
Current	50 Amps
Torque	84.4 Ft-Lbs
Speed	9550 rpm

Design Considerations

As was explained earlier, the objective of the design was to design a high power density motor with a good efficiency. This meant that the design had to maximize the power produced by the motor, minimize losses, optimize the weight, maximize the speed, and maximize the efficiency. Since the power depends on the motor voltage and the current, both of these needed to be large. The motor voltage depends on the magnetic flux density. To maximize this flux density, very strong magnets needed to be used. These magnets needed to have a special arrangement and the gaps between them needed

to be as small as safely possible. The current depends on the difference between the generator and motor voltages and on the resistance of the wire. This meant that while trying to keep the motor gap small, the generator gap had to be smaller by a big enough margin to yield a voltage difference that would produce a large current. Also, the wire used needed to have a low total impedance.

To maximize the speed of the test motor, a few things needed to be taken into consideration:

- Losses from the bearings needed to be minimized
- Friction losses between the disc and the stator needed to be minimized
- The auxiliary motor selected should be able to reach the desired speed with the load, test motor and generator, mounted to it
- The test motor to auxiliary motor pulley ratio would have to be optimized
- The vibrations in the rig would need to be low
- The temperature of all parts would have to be at an acceptable level

All of these factors had to be taken into account to maximize the speed of the motor because even though some of them do not affect the speed directly, they could make it necessary to shut down the motor during operation.

One downside to this design is that it results in high stresses on the rotating parts. This had to be taken into account in order to select appropriate materials for these rotating parts. In order to know what parts undergo the highest stresses, and exactly how large these stresses are, a stress analysis needed to be carried out.

Design Specifications / Materials Selection

Design specifications were made based on the considerations discussed in the previous section. A stress analysis of the rotating parts of the rig was carried out on the ANSYS program by Jeff Trudell at NASA. The permanent magnets are made from

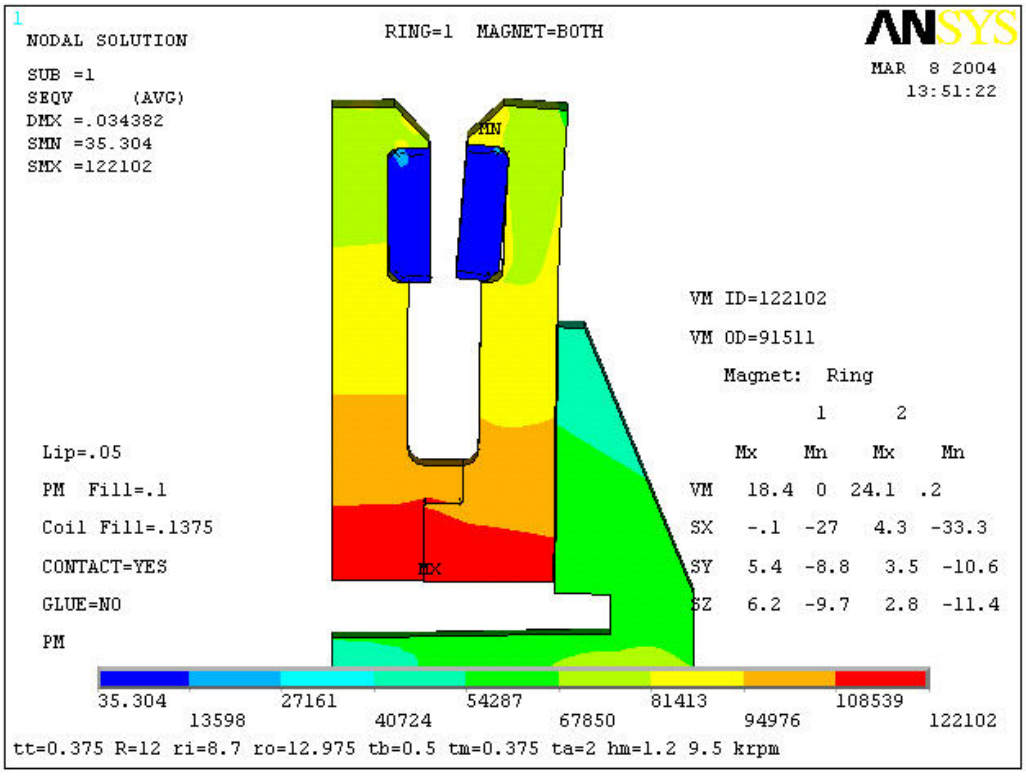

Fig. 4 Stress analysis of rotating parts

from Neodymium Iron Boron, 0.1 ft by 0.1 ft by 3/8 in thick. For a ¼ in air gap, they supply 1 Tesla of magnetic field. The permanent magnets would have a compressive stress of about 10 Ksi as shown in Fig. 4. This is well below the material's 160 Ksi yield strength. The magnets are arranged in a north-south-north-south sequence to maximize the magnetic field. The rotating back iron is made from ½ in thick heat treated 4340

low-alloy steel. The stress analysis (Fig. 4) showed that it would have about 120 Ksi hoop stress and this is well below the steel's 260 Ksi limit. The clamp and rotor are also be made out of 4340 steel. The stresses in the clamp and the rotor are much lower than those in the back iron so failure should not be a threat for them either.

Eddy current loss is controllable with stranded litz wire, leading to a high efficiency [5]. For this reason, litz wire was used in the stator and was compressed tightly into a thin, flat shape with epoxy and fiberglass to maintain its plate-like structure. The fiberglass used was garolite (G11) because it maintains its rigidity at relatively high temperatures. The fundamental switching frequency of the motor is the speed divided by twice the length of the magnet and is about 5 Kilohertz. The litz wire used was #38 wire, which is quoted to be able to handle 50 K hertz. This means that frequency related reactance would be small for this wire and would allow for higher currents.

The gaps between the magnets were set using shims that are made out of steel sheet metal. It was necessary to determine two gaps: the magnet – magnet gap for the motor to maximize the output voltage, and the gap for the generator based on a gap difference that was determined by the required voltage difference. The magnet – magnet gap was determined by calculating the flux density since the flux and the gap were found to be linearly related.

$$Gap \propto B \tag{1}$$

where B is the magnetic flux density. The flux density was calculated by dividing the required voltage by the required speed and the length of wire exposed to the magnet.

$$B = \frac{V}{vL} \tag{2}$$

where V is the voltage, i is the current, v is the velocity, and L is the length of wire. The motor - generator gap difference was determined by calculating the voltage difference from the resistance and the required current. This voltage difference was then used to determine the magnetic flux difference.

$$B_{motor} - B_{gen} = \frac{iR}{vL} \tag{3}$$

where R is the resistance of the wire and the *motor* and *gen* subscripts refer to the motor and generator respectively The gap difference could then be determined from the linear relationship between the magnetic flux and the gap size. This gap difference determined would be used initially but subject to change if the required voltage differences and currents were not met.

Rig Description

As briefly described earlier, the rig, shown in Fig. 5, is made up of a motor and generator assembly, both on the same rotor and shaft, an auxiliary motor, and containment chamber (housing). The housing includes a cylindrical ring and a base, which is made up of two flat circular pieces. The cylindrical ring has windows on the side that allow for adjustments to be made to the rig, and for the rotor – stator gaps to be checked without complete disassembly.

Fig. 5 Side view of rig

The motor and generator assembly are identical and are each made up of two magnetic discs with a stator in between them. Each magnetic disc consists of back iron and sixty four magnets arranged in a north-south-north-south array as is shown in Figs. 6 and 7. The discs either have keys or key slots (four on each side), depending on where they are used. The keys, located 90 degrees apart on the inner diameter of the discs, fit into key slots on other discs. The main function of the keys is to lock the magnetic discs together so that they all rotate as one. The discs also have threaded holes that are used during assembly to mount them onto the rotor.

Fig. 6 Magnetic disc

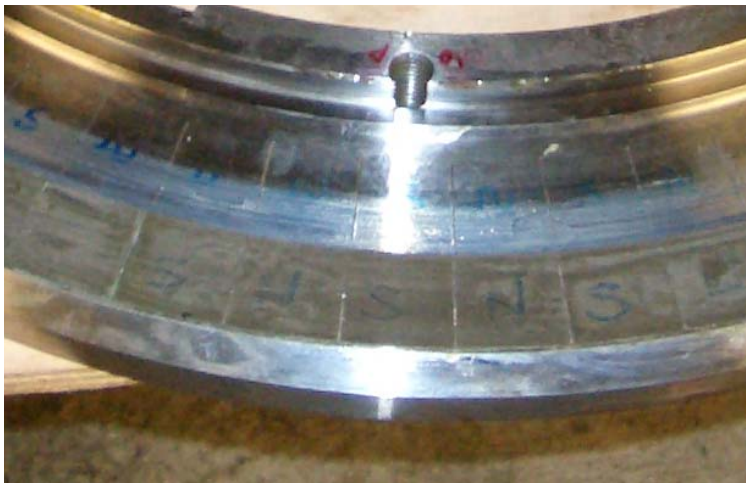

Fig. 7 North-South array magnet arrangement

The stator is made up of litz wire, high temperature epoxy, and fiberglass. The litz wire is tightly packed in slots on the fiberglass and is held in place by the epoxy. The epoxy is capable of withstanding very high temperatures up to about 400 ºF. This is to ensure that they do not disintegrate if and when the stators heat up during operation. The motor is a four phase motor, with the phases identified by A, B, C, and D. The stators are divided up into four quadrants, identified by 1, 2, 3, and 4, each having 16 wire slots for the wires for each phase. The wires are looped in and out of these slots, going back and forth until the end of the quadrant. The parts of the wires over which the

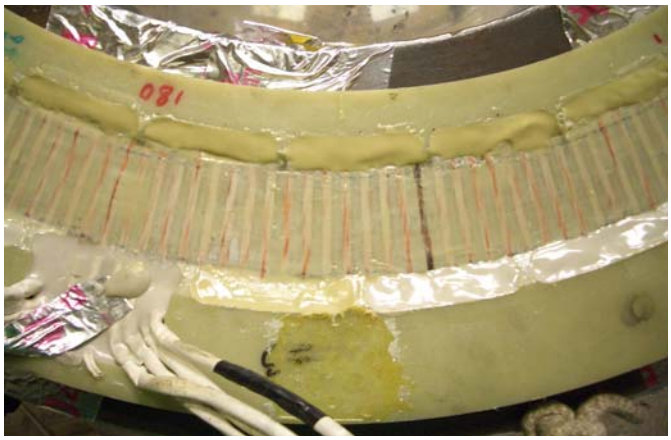

Fig. 8 Stator wires in fiberglass

magnets rotate are shown in Fig. 8. The ends of the wires from each quadrant extend out of wide slots on the stator. The slots, shown in Fig. 9, are filled up with the same high temperature epoxy discussed earlier. Thermistors that monitor the temperature of the stators are also cemented into these slots. The wires from each quadrant, extending out of the wide slots are connected by copper blocks, shown in Fig. 10. Each copper block

holds two wire ends, one from the end of one quadrant and the other from the start of the next. The wires are welded, by aluminum solder, into holes that were drilled in the copper blocks. Each phase has eight such blocks, equally divided between the motor and generator quadrants. The copper blocks are bolted to mounting blocks that are

Fig. 9 Wires extending out of wide stator slots

Fig. 10 Copper blocks with wire ends

bolted to the rig housing, 90 degrees apart, at the interfaces where two quadrants meet. The copper blocks connecting the motor quadrants are bolted to one side of the

mounting blocks and those of the generator are bolted to the other side, summing up to four copper blocks (one per phase) on each side, as is shown in Fig. 11. One end of the motor and generator wire series is connected by one of the copper blocks to close one side of the series loop. The other end is left open so that the circuit remains open. On one of the phases (phase A), wires are soldered to each of the open motor and generator ends and are connected to a relay, shown in Fig. 12. The wires are connected to each

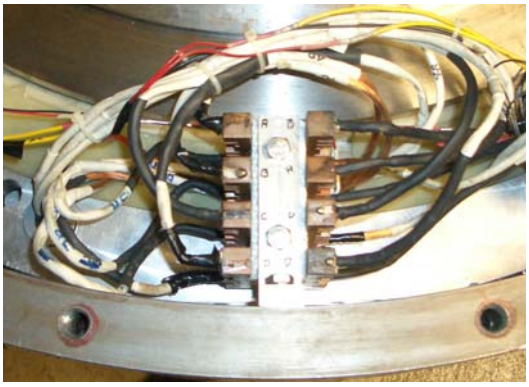

Fig. 11 Mounting blocks with copper blocks bolted to them

Fig. 12 Relay used to close the circuit

end of the relay such that the circuit is closed when the relay is powered up. A schematic of the wiring of phase A is shown in the Fig. 13. Phases B, C, and D are wired in exactly the same way except that the relay and the wires connected to points 1 and 2 are not included. The respective voltages are measured by soldering sensor wires across different points as follows:

- Motor voltage – 1 and 3

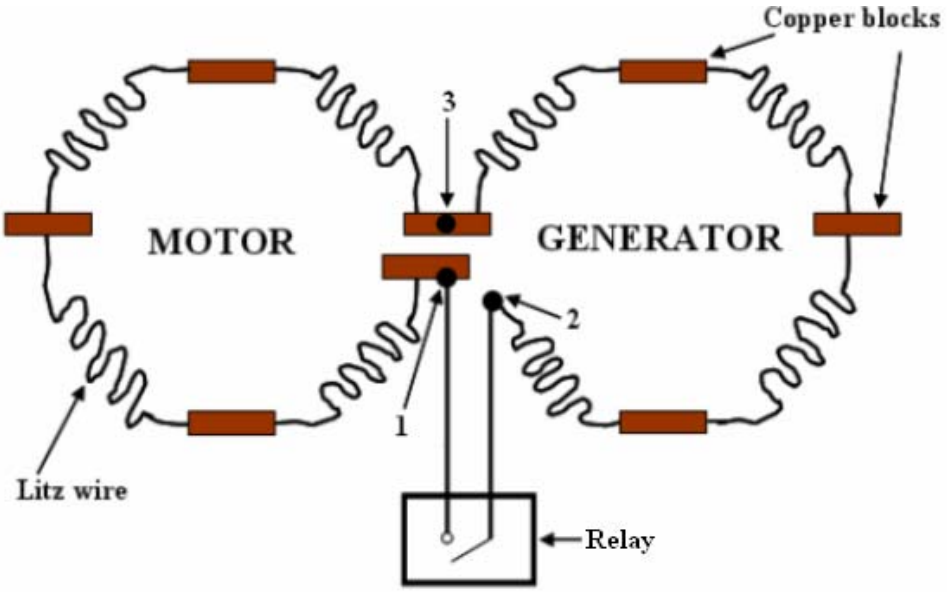

Fig. 13 Schematic of phase A wiring

- Generator voltage – 2 and 3
- Voltage Difference – 1 and 2

Hence, the ends of the sensor wires soldered to these points are connected to a scope or multimeter and used to read these values. When the circuit is closed for phase A, a current probe is used to read the current in the wire connecting either of points 1 or 2 to the relay.

The stators sit on aluminum rings that are held up by all thread rods. Fig. 14 shows the stator ring held up by strings above one of the aluminum rings. The rings can be moved up and down along the all thread rods to adjust the gaps between the stator and the magnets. A phase adjusting device is attached to the generator (bottom) stator that enables it to be rotated to adjust the phase between the motor and generator waveforms in open circuit and between the voltage and current waveforms in closed circuit. The nuts shown in the right picture in Fig. 15 go in the stator so that it moves with them. The

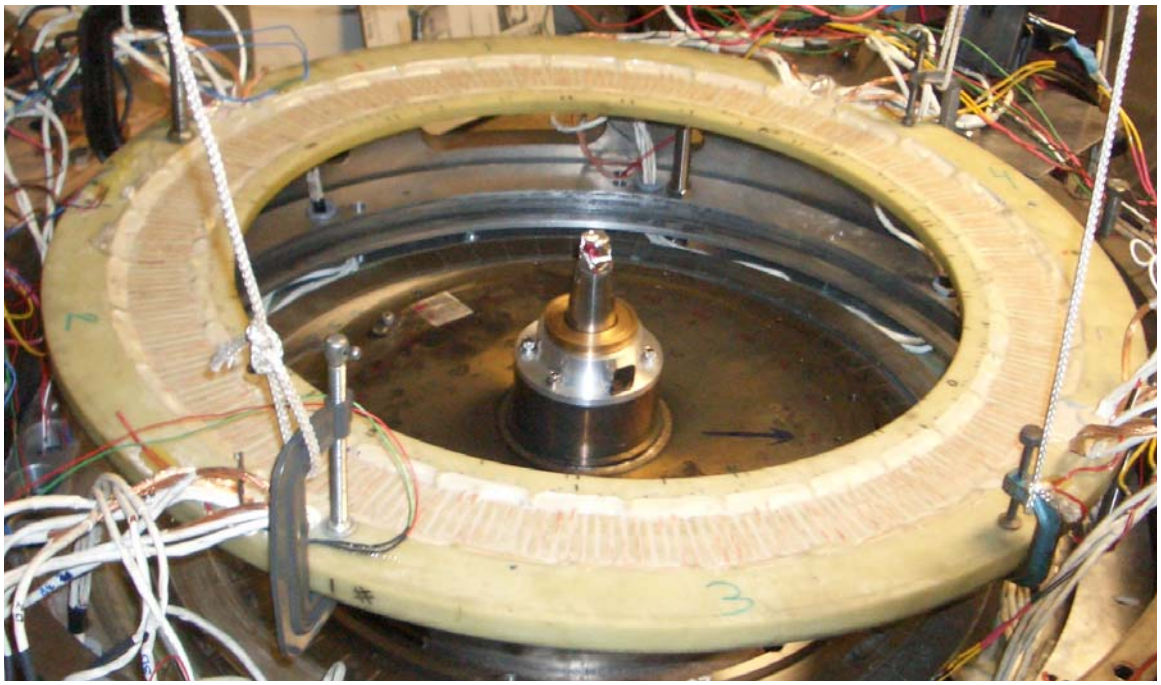

Fig. 14 Stator hanging above aluminum ring

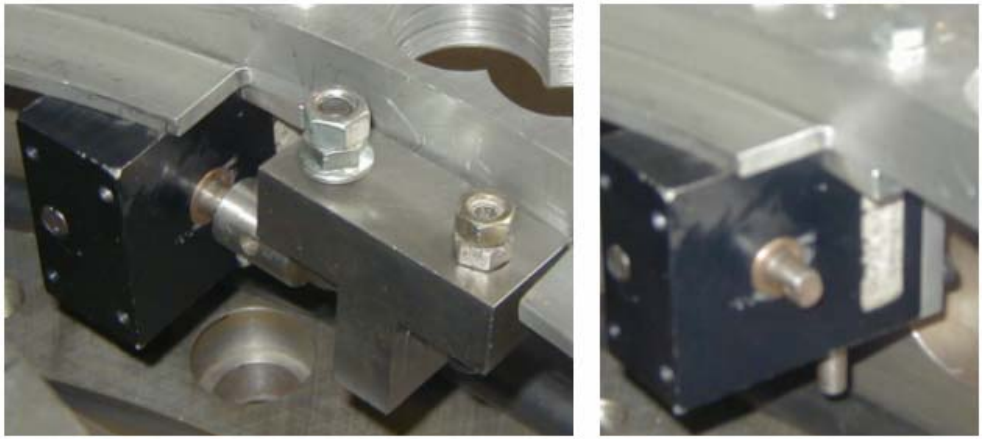

Fig. 15 Phase adjusting device

stator is moved by rotating the vertical shaft in the right figure, which causes the horizontal shaft to rotate. The cylindrical piece on the left figure is attached to the horizontal shaft by set screws so that they rotate together. The cylindrical piece holds a shaft that is threaded into the vertical part of the tee like piece. When the cylindrical piece is rotated, the shaft threads into the tee-like piece in the left picture, causing it to translate. This in turn moves the stator in the desired direction. As was stated earlier, the stators are mounted 180º out of phase in order to switch the current every time a wire crosses a magnet edge. Therefore, the generator stator is rotated, sliding along its aluminum ring, whenever the stators are not exactly at the desired phasing. The motor (top) stator however should not move during operation. Load cells, shown in Fig. 16, are used to monitor this. A steel block with slots that hold the load cells is bolted to the aluminum ring on which the stator sits. One end of another steel block is placed between the load cells while the other end is bolted to the stator, as is shown in Fig. 17.

Fig. 16 Load cells

Fig. 17 Load cell assembly

With this configuration, the steel block on the stator imparts a load on the load cells if the top stator undergoes rotation in either direction. The load cells are also used to measure the torque imparted on the stator when current is passing through the wires during closed circuit operation.

The magnetic discs are mounted onto the rotor and are separated by steel shims, one of which is shown Fig. 18. The rotor is centered by a shaft that is contained in a cylindrical housing and is held up by ball bearings. The bearings are secured by a housing that is bolted to the top and bottom of the shaft housing. Oil lubrication in the form of mist is pumped into the bearings through the top of the shaft and is sucked out at the bottom. The rotor centered by the shaft and the mist lubrication inlet port at the top of the shaft are shown in Fig. 20. A conical piece is attached to the bottom of the shaft giving it a conical base as was shown in Fig. 5. This conical base sits in a conical hole on a thick metal block that is bolted to the base of the rig housing. This metal block is shown in Fig. 19. Since the shaft, centering the rotor, sits in the metal block, the block

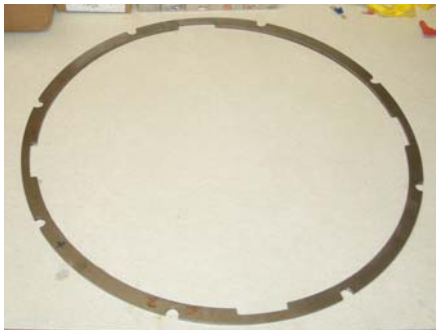

Fig. 18 Shim

Fig. 19 Metal block with conical hole

holds up the rotor weight, with the magnetic plates and the retainer clamps. 24 ¼ - 28 threaded holes are located 15º apart at the top and bottom of the rotor. These holes are used as locations for balance weights if / when there are vibrations due to imbalance during testing. The speed of the test motor is monitored by a Bently one-surround speed sensor. The sensor is bolted to the rig cover plate and is aimed at a steel sheet that is

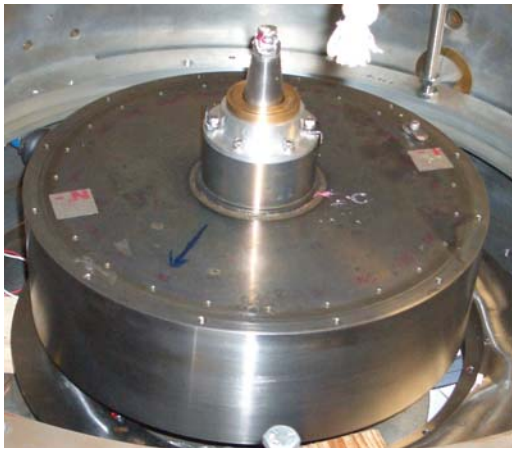

Fig. 20 Rotor and shaft

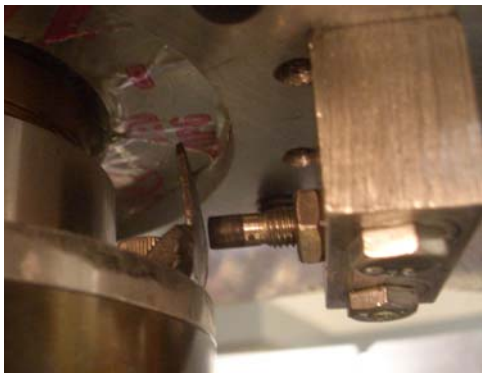

Fig. 21 Speed sensor aimed at steel sheet

bolted to the top of the shaft housing. Fig. 21 shows the sensor aimed at the sheet on the shaft. During rotation, the sensor picks up a signal every time the steel sheet crosses its path. This determines the speed of the sensor and records it to a Bently digital vector filter. Retainer clamps are bolted to the top and bottom of the rotor. These clamps, shown in Fig. 22, hold the magnetic discs in place to prevent them from sliding up or down along the rotor circumference. The clamps have four keys on their inner diameter that fit into the keyways on the magnetic discs. These keys on the clamp are shown in Fig. 23.

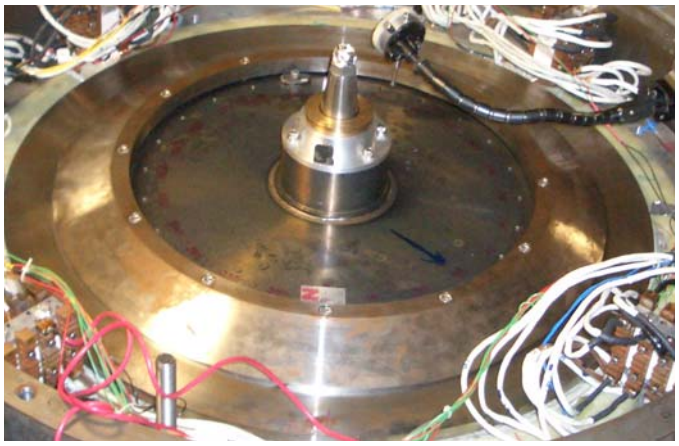

Fig. 22 Retainer clamps bolted to rotor

Fig. 23 Keys on retainer clamps

The rotor is rotated by an auxiliary motor that passes power to the rotor through pulleys and a belt. The rotor pulley is located at the bottom of the shaft, as shown in Fig. 5. The auxiliary motor is bolted to a mounting bracket that is bolted to two metal blocks. The blocks are mounted onto a shaft that is bolted to the bottom of the rig housing. These blocks swing along the shaft, making it possible to swing the motor back and forth in order to adjust the tension of the belt. An extension shaft, shown sitting on top of the

Fig. 24 Auxiliary motor and mounting bracket

motor bracket in Fig.24, is placed over the auxiliary motor shaft to extend it up to the height of the rotor pulley.

Spin Pit Specifications

The spin pit was designed by Randy Tucker to be able to test a variety of test rigs. Fig. 25 shows a drawing and some dimensions of the spin pit. It has the following parts and features:

- 5000 Watt-hour burst rated containment vessel
- Large opening automatic lid lift system for safe inspection and maintenance
- 10 horsepower (hp), 150000 rpm air turbine and 60000 rpm electric motor for shaft drive
- 75 hp, 120 pounds per square inches (psi), 300 standard cubic feet per minute (scfm) air compressor for turbine power

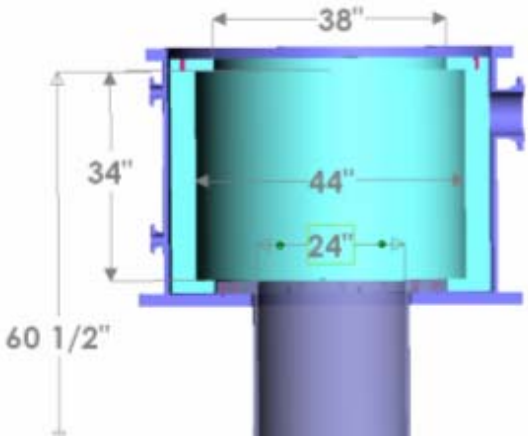

Fig. 25 Drawing and dimensions of spin pit

The lid lift system allows easy access to large dimension / weight test devices. The bottom stub section was designed for use with air table or test support area.

The lid lift system had the following features:

- 20000 pound capacity jack lift system
- Mechanical torque limiter on motor
- Current limiter on controller
- Support and containment dogs for additional work and test safety
- Top lid latch to lock lid in open position
- Positive pressure release system
- Safety shields for moving parts
- Alarms indicating lift operation and foreign object detection

MODELING AND PREDICTIONS

Electrical Model

The main output of the high power density motor developed is the power it can produce at the maximum speed of 10,000 rpm. This power was measured by taking the product of the voltage and the current and was compared to a power that is predicted in this electrical model. A schematic of the motor – generator circuit is shown in Fig 26.

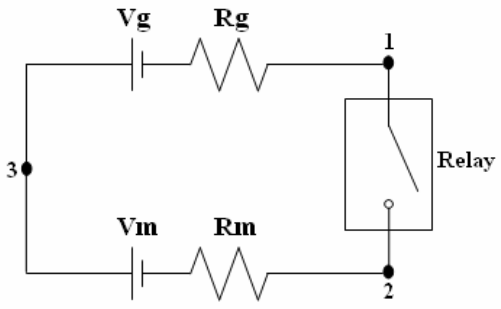

Fig. 26 Schematic of motor - generator open circuit

The predicted power was determined by taking the product of the predicted motor voltage, V_m in the figure, and the predicted current. This current would become active only when the circuit was closed, getting the circuit shown in Fig. 27. The motor and

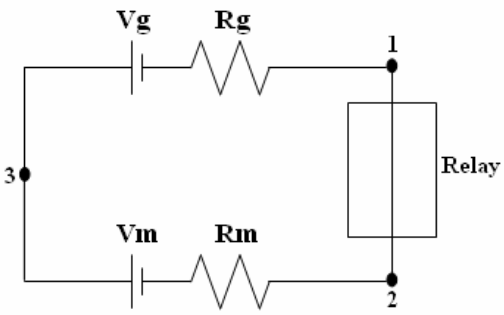

Fig. 27 Schematic for motor - generator closed circuit

generator voltages, measured across 2 – 3, and 1 – 3 respectively, were predicted using:

$$V = B * v * L \tag{4}$$

where V is the peak voltage, B the magnetic field, v the velocity, and L the length of the wire. This equation is determined from the fact that the force on the wire is the product of the magnetic field, the current, and the length of the wire, and that the power is a product of the force and the velocity, as well as the product of the current and the voltage. Hence:

$$F = B * i * L \tag{5}$$

$$P = F * v = i * V \tag{6}$$

where F is the force on the wire, i the current in the wire, and P the power. Substituting (5) into (6),

$$B * i * L * v = i * V \tag{7}$$

Now, dividing both sides by the current, i, equation (4) is derived. The current is predicted by dividing the voltage difference between the predicted motor and generator voltages, measured across 1 and 2 in the figure, by the resistance of the wires. The inductance of the motor and generator is small and so the difference between the voltages is just the combined IR (product of current and resistance) drop of the circuits. The magnetic field was predicted by a MATLAB model and is shown in Table 2, at room temperature for three different gaps. The model and predictions were done by Andrew Kenny. It can be seen from these values that there is a linear relationship between the total gap and the magnetic field. This means that a simple linear interpolation can be used to predict the magnetic field for other gaps. Using this

Table 2 Magnetic flux density and gaps

Total Magnet to Magnet Gap (inches)	Magnetic Flux Density (Tesla)
0.350	0.80
0.400	0.75
0.450	0.70

interpolation, the following relationship was derived:

$$B = 1.15 - Gap \tag{8}$$

Using this equation, the motor and generator fluxes, for the current magnet – magnet gaps of 0.32 inches in the generator and 0.368 inches in the motor, are 0.83 and 0.782 Tesla respectively. The length of the wire, *L*, is simply the parts of the wire that are exposed to the magnet and was determined by multiplying the width of the magnets by the number of wire slots in each phase. Hence, the length of the wire is

$$L = 0.1ft \times 0.3048\frac{m}{ft} \times 64 = 1.95m \tag{9}$$

The linear velocity can be determined by multiplying the radius of the magnetic discs by the angular velocity. Hence,

$$v = r\omega = 0.32m * 10000\frac{rev}{\min} \times \frac{2\pi}{60}\frac{rad}{s} = 335.1\,m/s \tag{10}$$

Therefore, the motor and generator peak voltages are:

$$V_{motor} = 0.782T \times 335.1\frac{m}{s} \times 1.95m = 510.99V \tag{11}$$

$$V_{generator} = 0.83T \times 335.1\frac{m}{s} \times 1.95m = 542.36V \tag{12}$$

The power output of the motor is evaluated using root mean square (RMS) values of voltages and currents. The RMS voltages can be determined from the peak voltage by dividing the peak voltages by a factor of the square root of two $\left(\sqrt{2}\right)$. Therefore, the motor and generator RMS voltages are:

$$V_{motorRMS} = \frac{510.99V}{\sqrt{2}} = 361.32V \tag{13}$$

$$V_{generatorRMS} = \frac{542.36V}{\sqrt{2}} = 383.51V \tag{14}$$

The difference between these voltages could then be used to determine the current and hence the power outputs expected from the motor. Therefore:

$$i = \frac{(383.51 - 361.32)V}{0.06\Omega} = \frac{22.19V}{0.06\Omega} = 369.83A \tag{15}$$

$$P = iV_{motorRMS} = 369.83A * 361.32V = 133813.10W \tag{16}$$

Hence, with rotor – stator gaps of 35 mils for the generator and 59 mils for the motor, the rig should have motor and generator voltages of 361.32 V and 383.51 V, a voltage difference of 22.19 V, a current of 369.83 A and a power output of 133.81 kW per phase at 10,000 rpm. Carrying out the same calculations for speeds from 1000 rpm to the first milestone speed of 5000 rpm, the same values were evaluated and are shown in Table 2. Plots of the predicted motor and generator voltages, voltage differences, currents and power output per phase versus speed are shown in Figs. 28, 29, 30, and 31. As can be seen from the plots, the predictions show that the motor and generator voltage, voltage

Table 2 Electrical predictions from 1000 to 5000 rpm

Speed (rpm)	$V_{motorRMS}$ (V)	$V_{generatorRMS}$ (V)	V_{diff} (V)	Current (A)	Power (W)
1000	36.13	38.35	2.22	36.98	1336.09
2000	72.26	76.70	4.44	73.97	5345.07
3000	108.40	115.05	6.66	110.95	12026.98
4000	144.53	153.40	8.88	147.93	21380.32
5000	180.66	191.76	11.10	184.92	33407.65

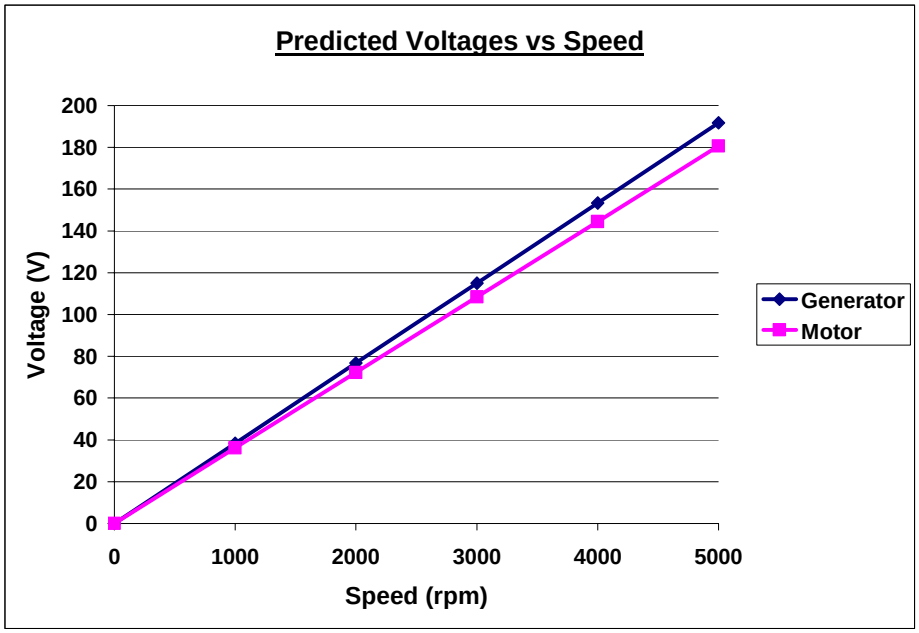

Fig. 28 Predicted motor and generator voltages

difference, and current should increase linearly with speed and the power output per phase should increase quadratically with speed.

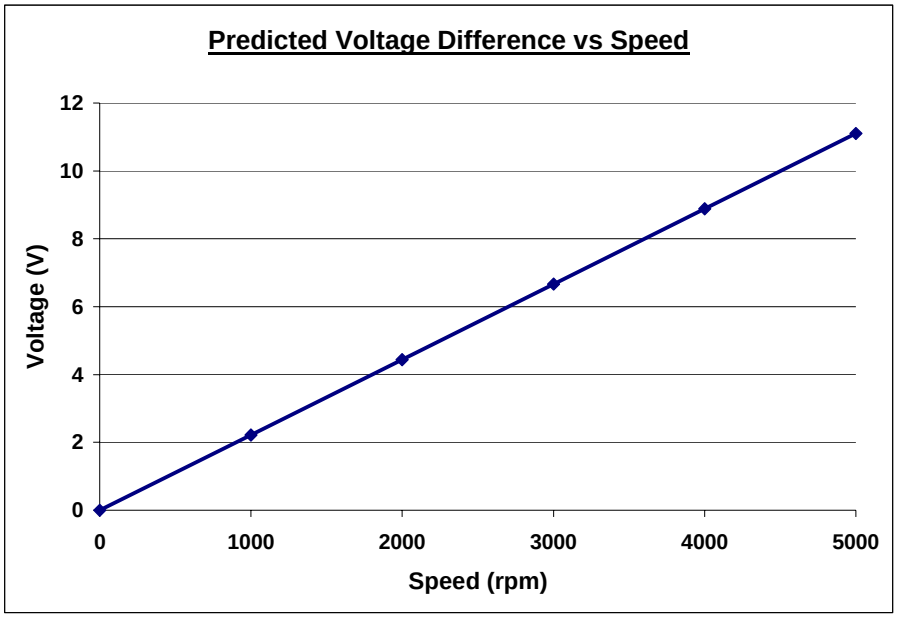

Fig. 29 Predicted voltage difference

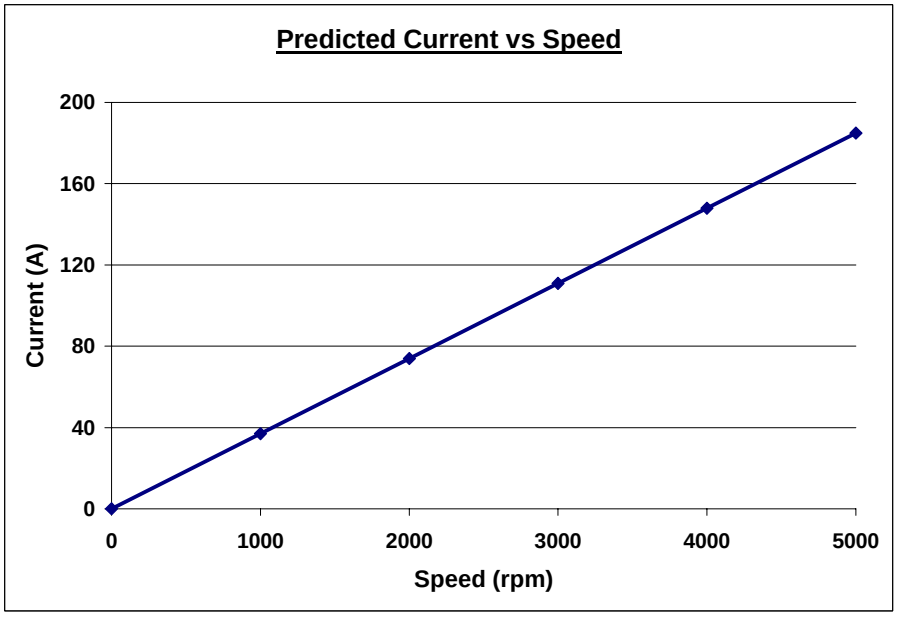

Fig. 30 Predicted output current

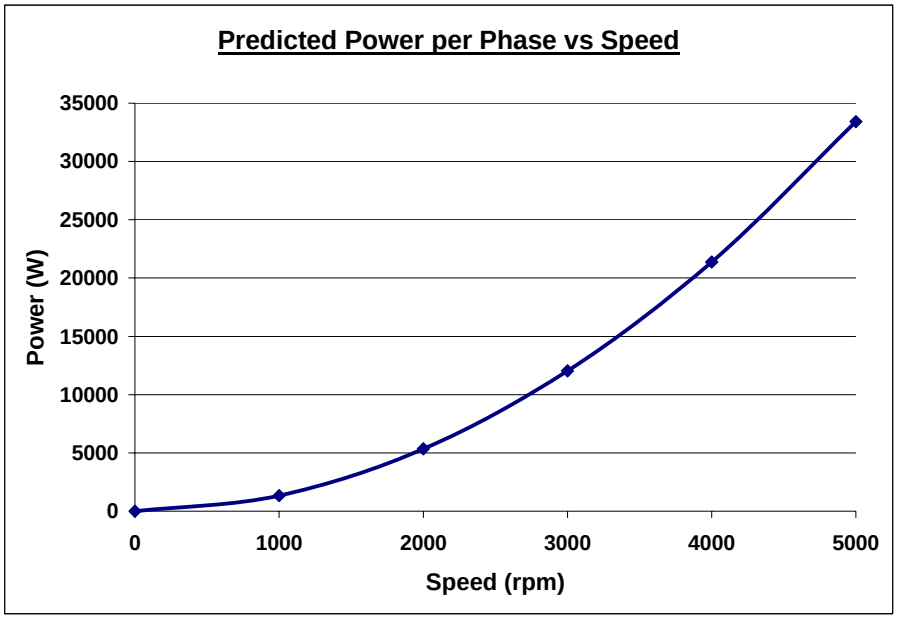

Fig. 31 Predicted power output per phase

Thermal Analysis

The first step in the thermal modeling was to approximate the power required to increase the temperature of the entire rig, including the housing, by a given amount, in a given period of time. This was done by assuming that the entire rig was a big block of low carbon steel. The power required to increase the temperature of a given mass, m, of a material by a given amount, ΔT, in a given time Δt is given by:

$$P = mc_p \frac{\Delta T}{\Delta t} \tag{17}$$

where P is the power required and c_p is the specific heat capacity of low carbon steels. Numerical values required for this calculation are:

$$m = 1000 lbm = 453.593 kg$$

$$c_p = 0.116 \frac{Btu}{lbm°F} = 485.344 \frac{J}{kgK}$$

Therefore the power required is:

$$P = 453.593kg \times 485.344\frac{J}{kgK} \times \frac{(\Delta T)K}{(\Delta t)s} \approx 220.15kW \cdot \frac{\Delta T}{\Delta t} \tag{18}$$

Hence, it would take approximately **220.15 kW** of power to increase the temperature of the entire blade tip rig by 1 K (1.8 ºF) in 1 second.

Next, the power required to increase the temperature of the stator by some value, ΔT, in a given period of time, Δt, was evaluated. The same equation was used, with the mass replaced by the product of the volume and the density of garolite (G11). This modifies the earlier power equation to:

$$P = \rho \cdot V \cdot c_p \frac{\Delta T}{\Delta t} \tag{19}$$

where ρ is the density of G11, c_p is the specific heat of G11, and V is the volume of the stator. The other variables are the same as defined earlier. For this case, the numerical values for the variables are:

$\rho = 1800\,kg/m^3$

$V = 159.36in^3 = 0.00261m^3$

$c_p = 990\,J/kgK$

Therefore, the power required is:

$$P = 1800\frac{kg}{m^3} \times 0.00261m^3 \times 990\frac{J}{kgK} \times \frac{\Delta T}{\Delta t} = 4.65kW \cdot \frac{\Delta T}{\Delta t} \tag{20}$$

This means that it would take a power of 4.65 kW to increase the temperature of one stator by 1 K (1.8 ºF) in 1 second. Next, the heat transfer into the stator and power losses due to windage were predicted for the rotor spinning at different speeds.

The stator was modeled by Fig. 32. Since the heat transfer was mainly into the

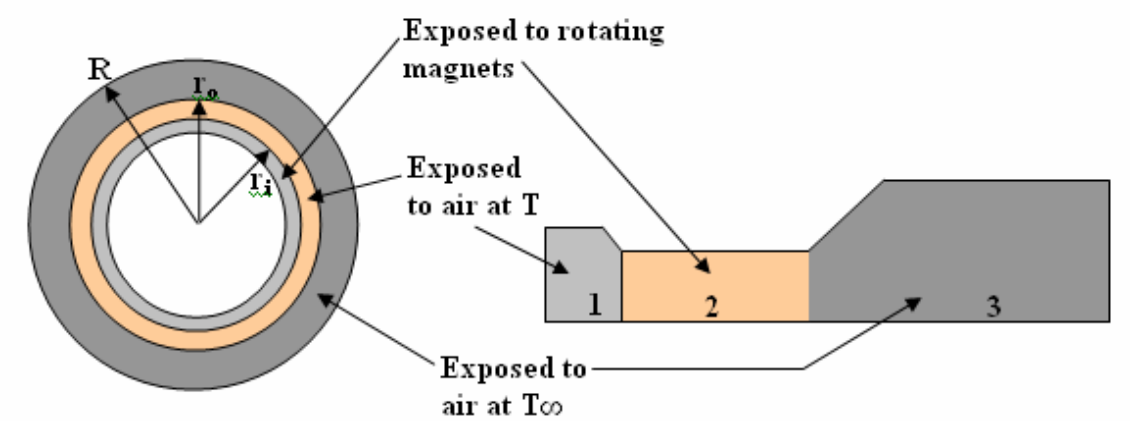

Fig. 32 Stator model showing top and cross sectional view

part exposed to the rotating magnets, an analysis was carried out to determine the temperature of part 2 of the stator at each speed. Also, with these, a steady state temperature of that part at different speeds could be evaluated. To do this, the model

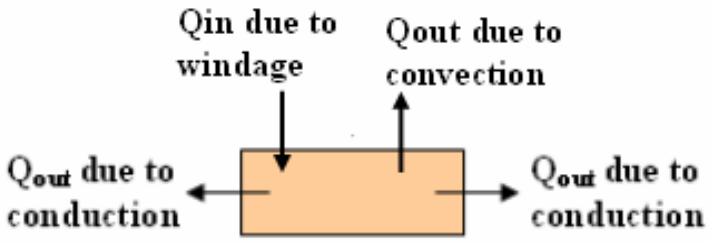

Fig. 33 Model for heat transfer to stator part

shown in Fig. 33 was used. Therefore, a heat transfer balance equation can be written as follows:

$$\rho V c_p \frac{dT}{dt} = Q_{in} - Q_{out}1 - Q_{out}3 - Q_{out}conv \tag{21}$$

where ρ is the density of G11, c_p is the specific heat, $Q_{out}1$ and $Q_{out}3$ refer to the conduction into parts 1 and 3 respectively. Because part 1 is so small and is assumed to be at the same temperature, T, as part 2, $Q_{out}1$ is assumed to be zero. $Q_{out}3$ depends on the temperature distribution in part 3 which will be assumed to be linear. The left end of part 3 that is in contact with part 2 is assumed to be at the same temperature, T, as part 2. The right end of part 3 is assumed to be at the ambient air temperature, $T\infty$. If the profile is assumed to be linear, the slope of the profile can be evaluated as:

$$slope = \frac{T - T\infty}{L} = \frac{T - T\infty}{R - r_o} \tag{22}$$

Therefore, the linear temperature distribution can be given as:

$$T = \left(\frac{T - T\infty}{R - r_o} \right) x + T\infty = \frac{Tx}{R - r_o} - \frac{T\infty x}{R - r_o} + T\infty \tag{23}$$

where x is the independent variable, starting at 0 and ending at $R - r_o$. The conduction in part 3 in the x direction is given by:

$$q_x = kA \frac{dT}{dx} \tag{24}$$

Therefore, the heat leaving part 2 into part 3 can be evaluated as:

$$q_x = \left(kA \frac{dT}{dx} \right)_{x=0} = kA \left. \frac{dT}{dx} \right|_{x=0} \tag{25}$$

The derivative of the temperature profile can be evaluated as follows:

$$\frac{dT}{dx} = \frac{1}{R - r_o} \left(x \frac{dT}{dx} + T \right) - \frac{T\infty}{R - r_o} \tag{26}$$

Now evaluating the heat conduction from 2 to 3 given (25):

$$Q_{out}3 = kA\left.\frac{dT}{dx}\right|_{x=0} = kA\frac{T}{R-r_o} - \frac{T\infty}{R-r_o} = kA\left(\frac{T-T\infty}{R-r_o}\right) \tag{27}$$

Now, to evaluate the heat leaving part 2 due to convection as the rotor rotates over it, a couette flow model is used. When a fluid is confined between two infinite parallel plates spaced *L* apart, and one of the plates is moving with the other stationary, the flow between them is called a couette flow. Therefore the heat leaving the stator to the air due to convection is given by the wall heat flux of a couette flow, given as:

$$q_s = \frac{k}{L}\left[T_s - \left(T_e + \Pr\frac{u_e^2}{2c_p}\right)\right][7] \tag{28}$$

where k is the thermal conductivity of G11, L is the rotor – stator gap denoted as h for this analysis, T_s is the steady state temperature, T, that the stator reaches when it is spinning at a constant speed, T_e is the temperature of the rotor assumed to be the same temperature, Tr, as the air between the stator and the rotating rotor, Pr is the Prandtl number of air, and u_e is the velocity of the rotating disc above the stator. With this, the heat transfer balance equation becomes:

$$\rho V c_p\frac{dT}{dt} = Q_{in} - kA\left(\frac{T-T\infty}{R-r_o}\right) - \frac{k}{h}\left[T - \left(T\infty + \Pr\frac{u_e^2}{2c_p}\right)\right] \tag{29}$$

If the speed of the rotor in rpm is increased linearly with time, an equation for T can be derived from (29) by simply solving the differential equation. When T is found, the temperature of the air, taking T_e to be the last known temperature of the rotor, can be evaluated as:

$$T_r = T_e + 0.5\left(T - T_e\right) + 0.22\left[\left(T_e + \Pr\frac{u_e^2}{2c_p}\right) - T_e\right][7] \tag{30}$$

With this, the steady state temperature, T, can then be evaluated as:

$$T = \frac{Q_{in} + \frac{kAT\infty}{R - r_o} + \frac{k}{h}\left(T_e + \Pr\frac{u_e^2}{2c_p}\right)}{\left(\frac{kA}{R - r_o} + \frac{k}{h}\right)} \tag{31}$$

The area, A, needed for the conduction from part 2 to 3 is determined by:

$$A = 2\pi r_o d \tag{32}$$

where d is the height of part 2. Next, the heat energy due to windage will be determined.

The heat transfer from the rotor into the stator due to windage could be determined either by treating the flow as a regular laminar flow or as a turbulent flow, depending on the Reynolds number. Using the regular laminar flow is obviously a more straightforward calculation and will be done first before the more complicated laminar or turbulent flow. The power input into the stator is given as:

$$P_{in} = \Gamma\omega \tag{33}$$

where Γ is the torque generated and ω is the spin rate in radians per second. The torque generated may then be given as:

$$\Gamma = \int_{r_i}^{r_o} d\Gamma = \int_{r_i}^{r_o} rdF \tag{34}$$

where dF is the differential force, and $d\Gamma$ is the differential torque. The differential force is defined as follows:

$$dF = \tau dA = \tau \cdot r dr d\theta \tag{35}$$

where τ is the shear stress on the stator, *dA* is the differential area, *dr* is the differential radial displacement, and *dθ* is the differential angular displacement.

The shear stress on the stator is defined as:

$$\tau = \frac{\mu r \omega}{h} \tag{36}$$

where μ is the absolute viscosity of air and *h* is the gap between the magnets and the stator. Therefore,

$$P_{in} = \Gamma\omega = \omega\int_{r_i}^{r_o} d\Gamma = \omega\int_{r_i}^{r_o} rdF = \omega\int_{r_i}^{r_o} r\tau dA = \omega\int_{r_i}^{r_o} r\frac{\mu r\omega}{h} rdrd\theta = \omega\int_{r_i}^{r_o} \frac{2\pi\mu\omega r^3 dr}{h} \tag{37}$$

Simplifying further,

$$P_{in} = \frac{2\pi\mu\omega^2}{h}\int_{r_i}^{r_0} r^3 dr = \frac{\pi\mu\omega^2}{2h}\left(r_0^{\,4} - r_i^{\,4}\right) \tag{38}$$

The values of the variables are given or measured as follows:

$\mu = 1.82\times10^{-5}\ Ns/m^2$

$\omega = 5000rpm = 523.60\,rad/\sec$

$h = 35mils = 0.035in = 8.89\times10^{-4}m$

$r_i = 11.4in = 0.29m$

$r_0 = 12.6in = 0.32m$

Plugging these in,

$$P_{in} = \frac{\pi\times1.82*10^{-5}\frac{Ns}{m^2}\times\left(523.60\frac{rad}{s}\right)^2\times\left(0.32^4 - 0.29^4\right)m^4}{2\times8.89*10^{-4}m} = 30.09W \tag{39}$$

Considering both sides of the stator, this power loss is doubled, giving a total power loss of 60.18W for a regular annular flow. The same calculation was repeated for speeds from 1000 to 4000 rpm and the power losses are shown in Table 3. These values for

Table 3 Laminar flow windage loss predictions

Speed (rpm)	Power loss (W)
1000	2.41
2000	9.63
3000	21.66
4000	38.51
5000	60.18

windage losses seem rather low and unrealistic though so the Reynolds number will be evaluated to determine the nature of the flow: whether it is laminar as already predicted or turbulent.

The Reynolds number is given by:

$$\mathrm{Re} = \frac{2\rho h}{\mu} V_0 \tag{40}$$

where ρ is the density of air and V_0 is the average swirl velocity across the gap

This average swirl velocity is

$$V_0 = \frac{r_i \omega}{2} \tag{41}$$

The Reynolds number is then expanded to

$$\mathrm{Re} = \frac{2\rho h}{\mu} V_0 = \frac{\rho h r_i \omega}{\mu} \tag{42}$$

The values for h, r_i, ω, and μ are the same as given in the earlier section and the density, ρ is $1.275\,kg/m^3$.

Plugging in these values,

$$\mathrm{Re} = \frac{1.275\frac{kg}{m^3} \times 8.89*10^{-4} m \times 0.29m \times 366.519\frac{rad}{s}}{1.82*10^{-5}\frac{Ns}{m^2}} = 6609.27 \tag{43}$$

As can be seen, the Reynolds number is greater than the transition value of 2300; therefore the air flow between the rotor and stator is turbulent.

Just like with the laminar flow, the power input into the stator is given by (33). The torque is given by:

$$\Gamma = \int_0^{2\pi}\int_{r_i}^{r_0} r dF = \int_0^{2\pi}\int_{r_i}^{r_0} r\tau_{rotor} dA = \int_0^{2\pi}\int_{r_i}^{r_0} r\tau_{rotor} \cdot r dr d\theta \tag{44}$$

For a turbulent flow, the shear stress, τ_{rotor} is defined as:

$$\tau_{rotor} = \tau_{stator} = \frac{\rho f(r)}{8} V_0^{\,2} \tag{45}$$

The term $f(r)$ is called the moody friction factor and is given by:

$$f(r) = 0.0055\left\{1 + \left[10^4 \times \frac{e}{h} + \frac{10^6}{\mathrm{Re}}\right]^{\frac{1}{3}}\right\} \tag{46}$$

where e is the surface roughness. Therefore, the torque is now given as

$$\Gamma = \int_0^{2\pi}\int_{r_i}^{r_0} r\tau_{rotor} dA = 2\pi\int_{r_i}^{r_0} r^2\tau_{rotor} dr = 2\pi\int_{r_i}^{r_0} \frac{\rho f(r)}{8}\left(\frac{r\omega}{2}\right)^2 r^2 dr \tag{47}$$

and the power input becomes

$$P_{in} = \Gamma\omega = \frac{\pi\rho}{16}\omega^3 \int_{r_i}^{r_0} r^4 \times f(r)dr = \frac{\pi\rho}{16}\omega^3 \int_{r_i}^{r_0} r^4 \times 0.0055\left\{1+\left[10^4 \times \frac{e}{h} + \frac{10^6}{\mathrm{Re}}\right]^{\frac{1}{3}}\right\}$$

$$= \frac{\pi\rho}{16}\omega^3 \int_{r_i}^{r_0} r^4 \times 0.0055\left\{1+\left[10^4 \times \frac{e}{h} + \frac{10^6}{\frac{\rho hr\omega}{\mu}}\right]^{\frac{1}{3}}\right\} \quad (48)$$

As can be seen, this integral is clearly very complex and will be quite difficult to carry out. This complex integral however, could be approximated using a numerical method called the Simpson's rule. Simpson's rule is defined as:

$$\int_{x_0}^{x_2} f(x)dx = \frac{H}{3}\left[f(x_0) + 4f(x_1) + f(x_2)\right] \quad (49)$$

H is the step between the variables and is given by:

$$H = \frac{x_2 - x_0}{2} \quad (50)$$

Therefore, the $f(x)$ from the Simpson's rule is replaced by an $F(r)$, which is defined as:

$$F(r) = r^4 \times 0.0055\left\{1+\left[10^4 \times \frac{e}{h} + \frac{10^6}{\frac{\rho hr\omega}{\mu}}\right]^{\frac{1}{3}}\right\} \quad (51)$$

Hence, the power input becomes:

$$P_{in} = \frac{\pi\rho}{16}\omega^3 \cdot \frac{H}{3}\left[F(r_0) + 4F(r_1) + F(r_2)\right] \quad (52)$$

The variables whose values have not been given previously are:

$H = 0.015m$

$r_1 = r_i = 0.29m$

$r_2 = 0.305m$

$r_3 = 0.32m$

$e = 4.5*10^{-5} m$

The power loss is then evaluated as:

$$P_{in} = \frac{\pi\rho}{16}\omega^3 \cdot \frac{H}{3}\left[F(0.29) + 4F(0.305) + F(0.32)\right] \tag{53}$$

Using these equations, $F(r)$ can now be evaluated as:

$$F(0.29) = 0.29^4 m^4 \times 0.0055 \times$$
$$\left\{1 + \left[\frac{10^4 \times 4.5*10^{-5} m}{8.89*10^{-4} m} + \frac{10^6 \times 1.82*10^{-5}\,\frac{Ns}{m^2}}{1.275\frac{kg}{m^3} \times 8.89*10^{-4} m \times 0.29m \times 366.519\frac{rad}{s}}\right]^{\frac{1}{3}}\right\}$$

$$= 3.89*10^{-5} m^4 \times \left\{1 + \left[506.187 + 151.065\right]^{\frac{1}{3}}\right\} = 3.77*10^{-4} m^4 \tag{54}$$

Carrying out the same operations for the other two steps,

$F(0.305) = 4.598*10^{-4} m^4$

$F(0.32) = 5.555*10^{-4} m^4$

The power is then evaluated as:

$$P_{in} = \frac{\pi \times 1.275\frac{kg}{m^3} * \left(366.519\frac{rad}{s}\right)^3}{16}$$

$$\times\frac{0.015m}{3}\left[3.77*10^{-4}+4\times4.598*10^{-4}+5.555*10^{-4}\right]m^4=170.82W \qquad (55)$$

Again, considering both sides of the stator, this power loss is doubled giving a total power loss of 341.64W for a turbulent flow. This operation was carried out for different gap sizes, some of which are shown in Table 4. These power losses are plotted against

Table 4 Model of power losses for variable gaps

Power Loss (Watts)	Gap (inches)
1037.250	0.001
621.314	0.005
500.382	0.010
441.648	0.020
404.510	0.030
378.070	0.040
357.842	0.050
341.640	0.060
261.93	0.070

the gaps for gap sizes ranging from 0.001 to 0.09 inches (1 to 90 mils) and are shown in Fig. 34. As can be seen from the table and figure above, the power losses due to windage are much larger for very small gaps but do not change that much as the gaps get bigger. The plot shows that this power loss would pretty much reach a constant value as the gap continues to get larger. This implies that increasing the gaps between the

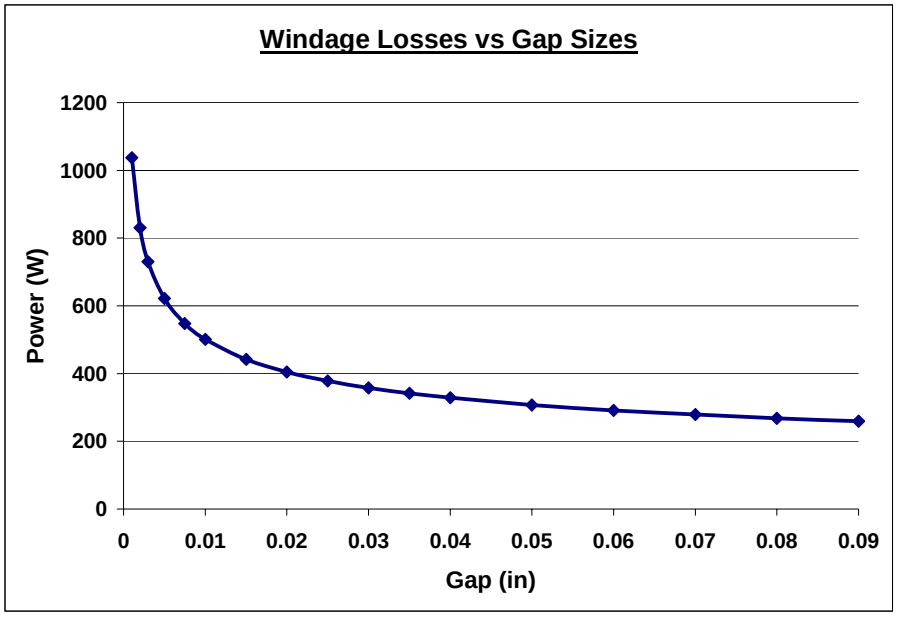

Fig. 34 Windage predictions versus gaps

magnets and the stator will not reduce the windage losses. This would mean that the heat energy going into the stator would not be substantially reduced and hence, the temperature of the stator will not increase that much more slowly.

The same calculations were carried out, varying the speed instead of the gap sizes. Values for each speed from 1000 to 5000 rpm are shown in Table 5. These values are plotted and shown in the Fig. 35.

Table 5 Model of power losses for variable speeds

Power Loss (Watts)	Speed (rpm)
9.07	1000
66.75	2000
217.49	3000
505.77	4000
975.97	5000

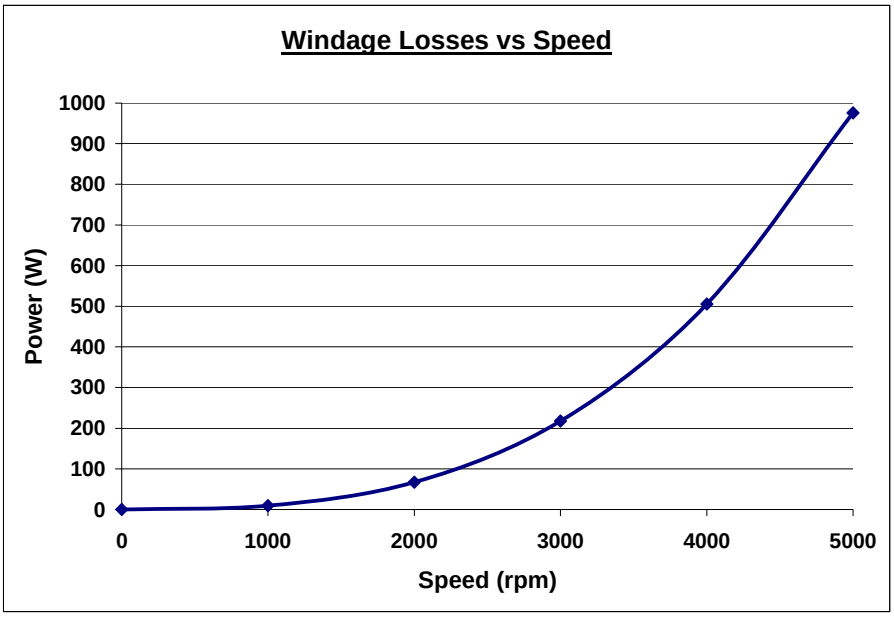

Fig. 35 Windage predictions versus speed

Next, the temperature of the stator will be evaluated at each speed by solving the differential equation given in (29). If the speed is assumed to be increased linearly with time from 1000 to 5000 rpm, in some time interval, T_p, the speed, and the windage

power losses can be expressed as functions of time. First of all, converting the speeds from rpm to rad/s, the speed can be expressed as:

$$u_e = r \cdot \frac{\omega}{T_p} t \tag{56}$$

Now, using these windage power loss values in table 5, the windage power losses can be plotted as a function of time and a curve fit can be used to derive an expression for this power loss as a function of time. This is done and is given as:

$$Q_{in}(t) = 0.0038t^2 - 0.7164t \tag{57}$$

Hence, with all of these known, the differential equation of T can be rewritten as:

$$\rho V c_p \frac{dT(t)}{dt} = 0.0038t^2 - 0.7164t - kA\left(\frac{T(t) - T\infty}{R - r_o}\right)$$

$$-\frac{k}{h}\left[T(t) - \left(T_e + \Pr\frac{\left(r\frac{\omega}{T_p}t\right)^2}{2c_p}\right)\right] \tag{58}$$

The variables needed that are not previously assigned are given as follows:

$k = 0.288 W/mK$

$A = \pi r_o^2 d = 2 * \pi * 0.32m * 0.0188m = 0.0378m^2$

$R = 0.38m$

$T\infty = 23°C = 296K$

$\Pr = 0.707$

$u_e = r_{middle}\omega = 0.305m * \omega$

Therefore, solving the differential equation in Maple, the temperature is given by:

$$T = T_e + 0.0021t + 3.702 \times 10^{-5} t^2 \tag{59}$$

When this temperature is known, the air temperature and the steady state temperature of part 2 of the stator can be evaluated at each speed using (30) and (31). The stator temperatures, air temperatures, and steady state temperatures evaluated, with a room temperature of 74 ºF, are shown in Table 6. Plots of these temperatures are shown in Fig. 36. In the plots, transient refers to the time dependent stator temperature when the speed is increased linearly to some value.

Table 6 Predicted stator and air temperatures

Speed (rpm)	Temperature (ºF)	Air Temperature (ºF)	S. S. Temperature (ºF)
1000	74.91	74.30	75.00
2000	79.74	77.90	80.89
3000	89.81	86.07	93.18
4000	107.05	100.74	114.04
5000	133.38	125.82	145.63

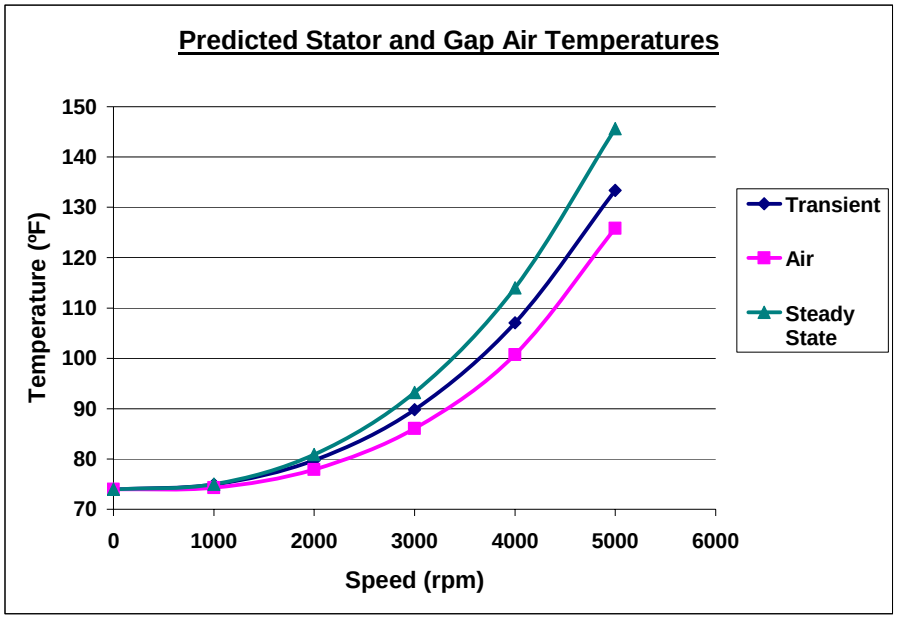

Fig. 36 Predicted stator and air temperatures

TESTING OF THE MOTOR

Assembly Procedures

The first step to testing the motor is the assembly and disassembly of the rig parts. The assembly procedures include the following:

1) The housing is assembled by bolting the two flat plates to the bottom of the cylindrical ring.
2) The cylindrical piece with the conical slot is bolted to the bottom of the housing base as shown in Fig. 37.

Fig. 37 Metal block bolted to housing base

3) The bottom retainer clamp is placed on the base of the housing.
4) Four all-thread rods are threaded into the holes in the base of the housing, located 90º apart, and secured with nuts.

5) The rotor with the shaft and conical base (Fig. 5) is dropped down into the conical slot from (2), making sure that they go through the hole in the retainer clamp
6) The bottom retainer clamp is bolted to the bottom of the rotor.
7) One nut is threaded down each of the all-thread rods from (4) to about the height of the top of the magnetic disc.
8) The bottom aluminum "stator holder" ring (ring 1) is slid down the all thread rods until it sits on the nuts.

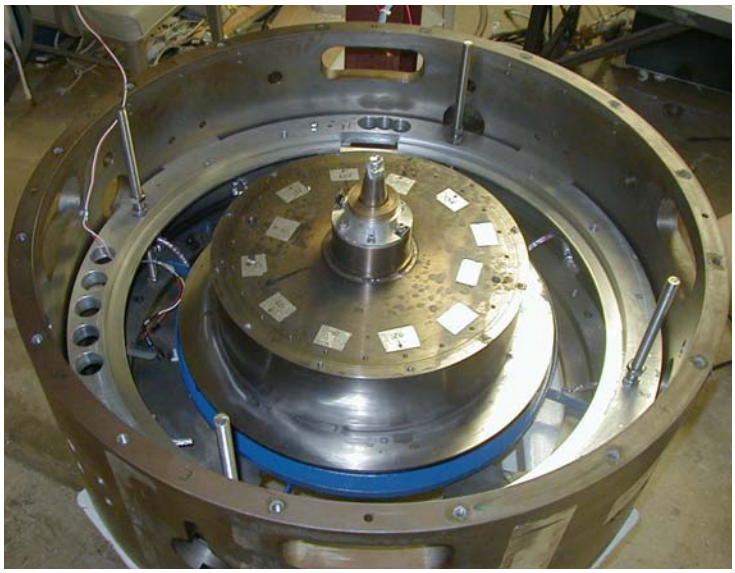

Fig. 38 Assembly with no discs

9) Never-seez is applied on the rotor as a lubricant to make it easy to slide parts down the side of the rotor. Fig. 38 shows the rig assembly up to this step.
10) The bottom generator magnetic disc (disc 1) is lowered down along the rotor till it rests on the retainer clamp, and its keyways lock with the keys on the clamps. The side holding the magnets points upwards. To lower the disc, four all-thread rods are

threaded through the holes on the inner diameter of the disc. The rods go through far enough so that they sit on the clamp with the bottom of the disc flush with the top of the rotor. The all thread rods are then threaded out slowly until the disc rests on the clamp. The assembly with disc 1 installed is shown in Fig. 39.

11) Two nuts are threaded down each of the all thread rods. One is taken all the way down till it hits ring 1 and the second one is set about one inch above the first one.

Fig. 39 Assembly with disc 1

12) The generator stator is placed in its slot in ring 1 so that the part holding the wires is over the magnets.

13) The shims are put in; lowering them down along the rotor till they sit on the inner diameter of the magnetic disc, and making sure that the holes and keyway slots match the holes and keys on the disc.

14) The top aluminum “stator holder” ring (ring 2) is slid down the all thread rods until it sits on the nuts. Fig. 40 shows the assembly up to this point.

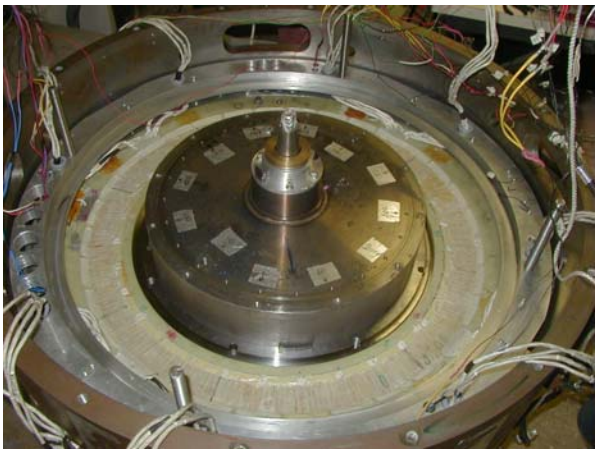

Fig. 40 Assembly with stator 1

15) The top generator magnetic disc (disc 2) is lowered down along the rotor till it rests on the shims and its keyways fall into the keys on disc 1. The side holding the magnets points downwards over the stator wires as is shown in Fig. 41. The disc is lowered using the same procedure as for disc 1, except in this case, the all thread rod ends should sit in the circular slots on the inner diameter of disc 1.

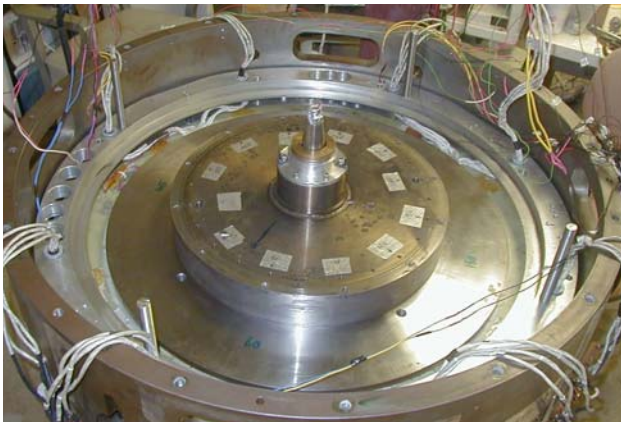

Fig. 41 Assembly with disc 2

16) The bottom motor magnetic disc (disc 3) is lowered, magnets facing upwards, down along the rotor till it is back-to-back with disc 2. The same lowering procedures are followed but with the all thread rods sitting on the back of disc 2.
17) Steps (12), (13), and (15) are repeated the top stator (stator 2), the shims, and the top motor magnetic disc (disc 4)
18) The top clamp is bolted to the top of the rotor, with its keys going into the keyways on top of disc 4.
19) The mounting blocks are bolted to the inside wall of the housing cylindrical ring. The blocks are located 90º apart.
20) The copper blocks holding the wire ends are bolted to the connecting blocks.
21) The load cell assembly is put in, bolting the respective parts to the housing ring and the top stator.
22) A top cover plate, shown in Fig. 42 is placed over the housing. The plate has through holes that allow the four all thread rods to pass through them. Nuts are then threaded down the all thread rods and tightened to secure the cover plate.
23) All the sensor wires from the thermistors and from each of the phases are passed through the holes on the cover plate and are placed on top of the plate.

Fig. 42 Assembly with top cover plate

Determination of Stator Current and Temperature Limit

A test was carried out by Randy Tucker to determine the maximum allowable currents and temperatures for the stator. In the test, a piece of the stator material, G11 with the wires looping in and out through their slots was used. A clamp-on welding machine was used to pass currents through the wires in the stator. The current was gradually increased until bending was noticed in the stator. The bending in the stator was caused by the wires getting to a temperature where they began to expand. Because the wires are so tightly fitted into the slots on the G11, the expansion of the wires caused the G11 material to bend downwards. A schematic of the cross section of the wires in the stator before and after the expansion of the wires is shown in Fig. 43. This test was repeated multiple times until a consistent current and temperature limit were reached. It was found that when 150 A of current was passed through the wires, they reached a

temperature of 155 ºF and started expanding, causing the stator material to bend downwards.

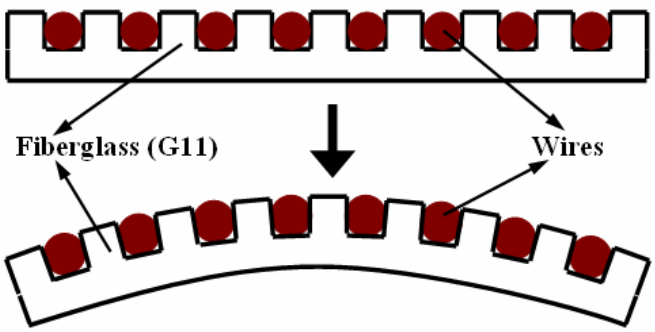

Fig. 43 Stator current / temperature limit test

Test Variables and Measuring Devices

The main variables monitored were the time, speed, motor and generator voltages, current, vibrations, and temperatures of different parts of the rig. The time is measured using a stop watch. The speed is measured by a Bently one-surround sensor that is aimed at the motor shaft as was shown in Fig. 21. The sensor is connected to a proximitor (Fig. 44) that connects it to a 24 volts power supply (Fig. 45), and to a digital

Fig. 44 Proximitor for speed sensor connection

vector filter that displays the speed in rpm. The filter is shown in Fig. 46. The motor and generator voltages are measured by an oscilloscope or a multimeter, and their

Fig. 45 Power supply for speed sensor (top) and accelerometers (bottom)

Fig. 46 Digital vector filter (top) and oscilloscope (bottom)

waveforms are plotted on the oscilloscope. The current is measured by a Tektronix clamp-on current probe shown in Fig. 47. The probe is put on one of the wires that connects the motor / generator wire ends to the relay. The output from the current probe

is read by the oscilloscope shown in Fig. 46. The temperatures of the stators and the bearings are measured by thermistors that are cemented, or taped on to them. The

Fig. 47 Clamp-on current probe

thermistors are all connected to a switch box that is connected to a temperature readout device. The thermistors are connected to the switch box such that each number on the

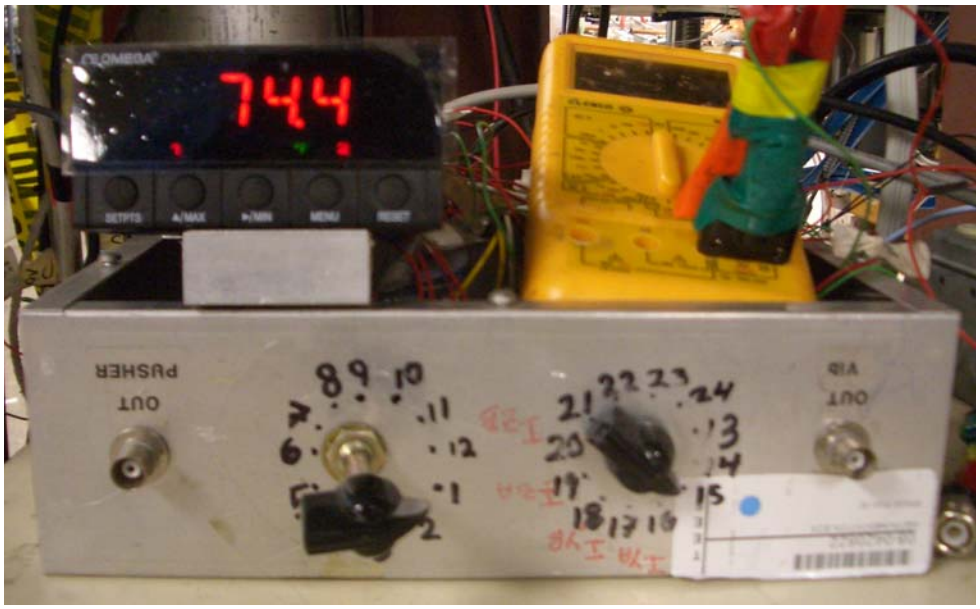

Fig. 48 Switch box and temperature readout device

box represents one thermistor. The switch box and temperature readout device are shown in Fig. 48. The vibrations are measured by accelerometers that are waxed to the outside wall of the rig housing. One accelerometer is at the top and the other at the bottom on the same vertical position. The accelerometers are powered by a Kistler accelerometer power supply, shown in Fig. 45 and their numerical outputs are displayed on the digital vector filter. The digital vector filter is normally set to only display numerical values for vibrations at the spin frequency. For this reason, the accelerometers outputs are made to be displayed on the oscilloscope too, in the form of peak vibrations and the frequencies at which they occur. This monitors vibrations that may occur at frequencies other than the spin frequency.

Test Setup and Procedures

Testing of the motor was primarily done in the spin pit. In order to begin the testing, the rig was bolted to the spin pit flange, as is shown in Fig. 49. The air input and output, as well as the lubrication for the motor bearings were turned on. The flange, with the blade tip was then lowered into the pit and bolted down. Fig. 50 shows the top

Fig. 49 Test rig bolted to spin pit flange

of the spin pit flange with the test rig secure in the pit. With the rig in the pit, the fuses for the control of the auxiliary motor drive were plugged in and the controller was turned on. After all the parameters on the drive had been verified, the motor was ready to be tested. Testing starts when the auxiliary motor is turned on, and its speed gradually increased. The speed of the auxiliary motor was monitored by the readings shown on its drive while the speed of the rig was monitored by the output of the speed sensor displayed on the digital vector filter. Times, speeds, open circuit voltages, vibration displacements, and temperatures were monitored and recorded at various speeds. The speed was gradually increased, while ensuring that the vibrations and temperatures were at acceptable levels. The maximum allowable vibration displacement was 0.2 in/s. At

Fig. 50 Spin pit lid with test rig in pit

any desired speed, the relay was turned on to close the circuit so that closed circuit voltages and currents could be measured. Testing was stopped simply by stopping the auxiliary motor controller and allowing the motor to slow down. This was done when all the required data for that particular test had been recorded. Shut down was also necessary when there seemed to be an emergency such as reaching any of the limits (vibration or stator temperature), hearing unusual sounds, or perceiving unusual smells.

Problems and Modifications

One major problem that was encountered during testing was that the rig had vibrations at frequencies other than the spinning frequency. In other words, there were

vibrations at the spinning frequency as well as at multiples of the spinning frequency. The vibrations at the spinning frequency were mostly or entirely due to imbalance and could be suppressed or eliminated by placing balance weights at different positions on the rotor to account for the imbalance. The size and positions of these balance weights were determined using a MATLAB balancing code. It was difficult to determine with certainty what the causes of the other vibrations were. It was suspected that one possible cause was that there were slight movements of parts of the rig that came loose or were not fastened securely enough. One possibility for this looseness was the retainer clamps that were bolted to the top and bottom of the rotor and held the magnetic plates between them. It was possible that these retainer clamps were vibrating because there wasn't enough torque applied to the bolts that were used to fasten them to the rotor. This could have been as a result of the bolts loosening up or stretching. Higher rated bolts were acquired to account for this and a larger torque was applied to them.

Another possible cause of these vibrations was that the auxiliary motor was vibrating and causing the test motor and generator to vibrate. To suppress this, additional brackets were made for the auxiliary motor, so that it was held more securely. Also, the extension shaft that was used to get the auxiliary motor pulley to the height of the rotor pulley may have been causing a slight swing. To eliminate this, a big hole was made in the bottom of the rig housing so that the auxiliary motor could be moved higher up, with part of it going into the housing. This was done to get its shaft to be at the height of the rotor pulley so that the extension shaft was no longer necessary.

The second major problem that was faced during the testing was that of the stator temperature increasing too rapidly as the speed of the rotor was increased. This was a problem because the stator was getting to the temperature limit before it was possible to get to the target speed of 5000 rpm. This rapid temperature increase could be as a result of windage or eddy currents losses. However, as was explained in an earlier section, the stranded litz wire configuration was employed to have low or zero eddy current losses. This meant that most of the temperature increase was as a result of windage losses. This would mean that the stators, the discs, and the air in the gap between them were getting hot due to the friction imparted by the rotation. There seemed to be very little heat transfer from the stator to the environments, mainly because surrounding parts were also hot, and because the stator material, G11, has a low thermal conductivity. As a result, while most of the heat generated due to friction was being stored in the stator, more was being added as the speed was increased.

To reduce the rate of increase of the temperatures of the stator, two approaches were taken: reducing the starting temperature of the stator and creating a temperature gradient in the rotor - stator gap. To reduce the starting temperature, the original air input mechanism for the rig was replaced by a window unit air conditioner. An insulated hose was connected from the air conditioner to the top of the rig housing where the air inlet port used to be located. This meant that the air going into the top of the rig would change from room temperature to about 60 °F (the minimum temperature the air conditioner could reach). With this, the air input could be turned on hours before testing

began so that when testing started, most or all of the parts in the rig would be at a temperature much lower than room temperature.

In an attempt to create a temperature gradient in the gap, cold air was pumped into the gaps from the outside circumference of the stator. To do this, an air injection system was designed. The air injection system included a high pressure air source, a heat exchanger to cool the air, thick plastic hose to transport the air into the rig, and

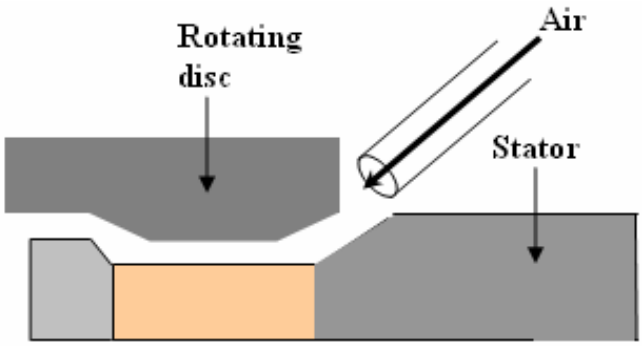

Fig. 51 Schematic of air injection into gaps

narrow flexible rubber tubing to blow the air into the gaps. The heat exchanger was made by inserting a coiled copper tubing into a cold water bath and pumping the air through the copper tubing prior to its entrance into the rig. The thick plastic hose made a ring around the top and bottom stators. Some more of this plastic hose was used to connect the outlet of the heat exchanger to the hose ring around the top stator, and to connect the top hose ring to the bottom hose ring. The narrow tubing was attached to the hose rings at different points on the circumference and aimed into the rotor – stator gap as is shown in Fig. 51. Hence, when the air source was turned on, the air would through the copper coils, to the connecting hoses, into the hose rings, out the ends of the rubber

tubing and into the gaps. The ends of the narrow rubber tubing were oriented at an angle almost tangential to the direction of rotation so that the air was blown out almost parallel to the discs. This was done because Etemad et al. found that it was the most effective way to get air into gaps between rotating parts [8]. Testing was done with this modification and it was discovered that it did not cause much improvement. It was suspected that this was because during rotation, the air already in the gaps was being pushed out due to centrifugal force, thereby, stopping air from coming in from that direction. This prompted the idea that it would be more effective to force air into the gaps somewhere along the radius of the discs. If cold air was forced into the gaps somewhere along the radius, then the hot air would be forced out on the outer circumference due to centrifugal force. This would be similar to the operation of a Tesla pump, shown in Fig. 52. In the figure, the air goes in through the blue colored section and goes out on the circumference in the red colored section.

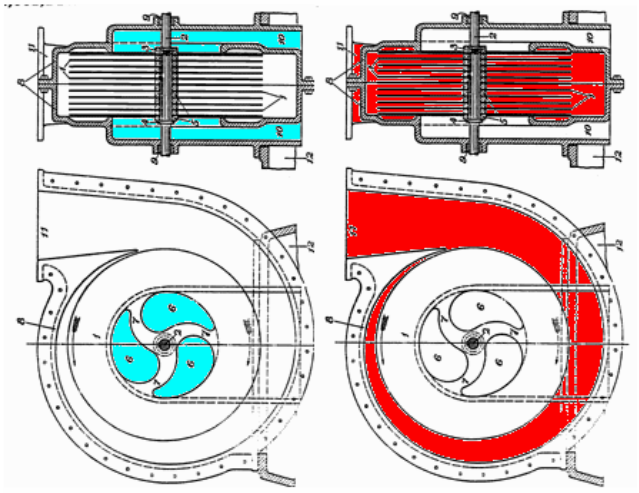

Fig. 52 Schematic of a tesla pump [9]

To imitate this Tesla pump, holes were drilled in the discs, away from the magnets. As is shown in Fig. 53, the holes in the disc are not very big and so will

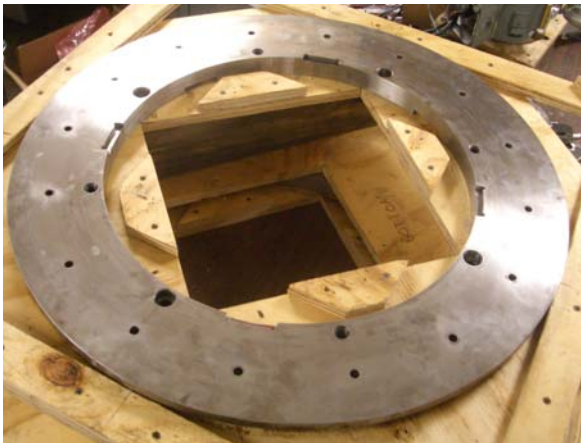

Fig. 53 Magnetic disc with holes

probably not allow as much air in as the actual tesla pump would. Troughs were made and placed above the holes and cold air was pumped into the troughs from a heat exchanger. The troughs are shown above the discs in the Fig. 54. The vertical walls of

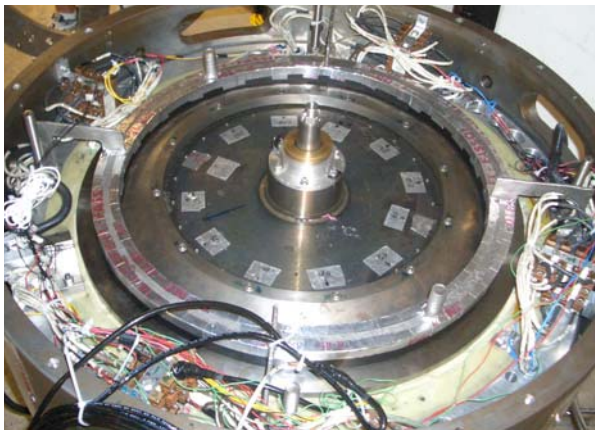

Fig. 54 Trough hanging over the holes

the troughs were lined with plastic shim material which was set really close to the rotor surface. This was done for two reasons: to have the cold air pumped directly above the holes with not too much leaking out, and to stop particles or metallic chips from getting down into the holes. It was assumed that the pressure in the parts of the gaps that align with the holes was very low because the air was being pushed to outer parts by centrifugal force. With this low pressure, and the high pressure of cold air in the troughs above the holes, the cold air could travel into the holes due to the pressure gradient. This cold could then travel outwards, to the gap between the stator and the magnets and then out the sides like in the tesla pump.

Another major problem encountered was that the test motor was limited to about 4000 rpm because the auxiliary motor was unable to go any further. This problem was first encountered with the old auxiliary motor. The old motor was a 5 hp, 5000 rpm motor so it seemed logical that it could not get to 5000 rpm, since some of its power capacity was being used to overcome losses. A new highly rated auxiliary motor was installed. The motor was a 25 horsepower, 25000 rpm, constant torque motor. This motor was much more powerful and required more accessories for its operation. It had a water jacket that required two hoses pumping water, one going in and the other going out. It also had a lubrication inlet and outlet. With all of these, the motor would not run hot and would not suffer significant bearing power losses. The water jacket was also an additional benefit because being so cold; it would draw some of the hot air away from the rig. A hat shaped piece was made as a mounting bracket for the motor and additional steel brackets were made, one for each side, to provide more rigidity when the auxiliary

Fig. 55 New auxiliary motor

motor was mounted. Six slots were cut in the hat shaped piece. They were used as through holes to mount the motor to the bottom of the rig housing. The slots were made instead of regular through holes because they were used as an easy means to tighten the belt. The new aux motor and its mounting assembly are shown in Fig. 55. The motor was simply slid backwards as far as was required to tighten the belt and was held in that position until the bolts were tightened. An encoder was also installed on the motor shaft to allow the motor to have a feedback system. Without this encoder, the motor would not be able to track its exact speed but would report whatever input command was given to it by the controller. The new and more powerful auxiliary motor handled the rig losses better. It still did not seem to be providing enough power to handle the load of the motor and the losses. With this, the resolution was to make the auxiliary motor provide more power by installing a smaller pulley in order to increase the rotor to auxiliary

motor pulley ratio. The ratio was increased from about 1.5:1 to about 2:1. This meant that the auxiliary motor would be spinning at twice the motor speed but would be providing more power at each speed and hence doing less work. That is, since the motor is a constant torque motor,

$$P = Tw \Rightarrow T = \frac{P}{\omega} = \text{constant} \tag{60}$$

and is rated as 25 hp, 25000 rpm motor, it has a 1:1 hp to 1000 auxiliary motor rpm ratio. Hence, by increasing the pulley ratio to 2:1, the auxiliary motor would be spinning at twice the speed of the rotor. The available power would increase from 1.5 hp to 1000 rotor rpm to 2 hp to 1000 rotor rpm.

The power losses that the rotor had to overcome were due to windage and drag forces. To reduce the drag and windage losses between the rotor and stator, the stator surface over which the rotor rotates was smoothened and polished. Holes and inconsistencies on areas around the rotation path were also filled up as can be seen in the bottom pictures in Fig. 56. These were done because the rough surface and the presence of these holes were discovered to be possible sources of drag from a paper by Zimmermann et al. They pointed out that "friction losses of rotating discs are often increased by protruding bolt heads and surface imperfections" [10]. The surfaces were smoothened by putting a thin flat layer of high temperature epoxy over the entire rough stator surface, lightly sanding the surface with a grinder and then polishing the surface with a polishing wheel. To fill up the holes on the outside parts, the protrusions were grinded off first. The same high temperature epoxy was then applied, putting a little more than was needed and then leveling it off with flat plastic sheets.

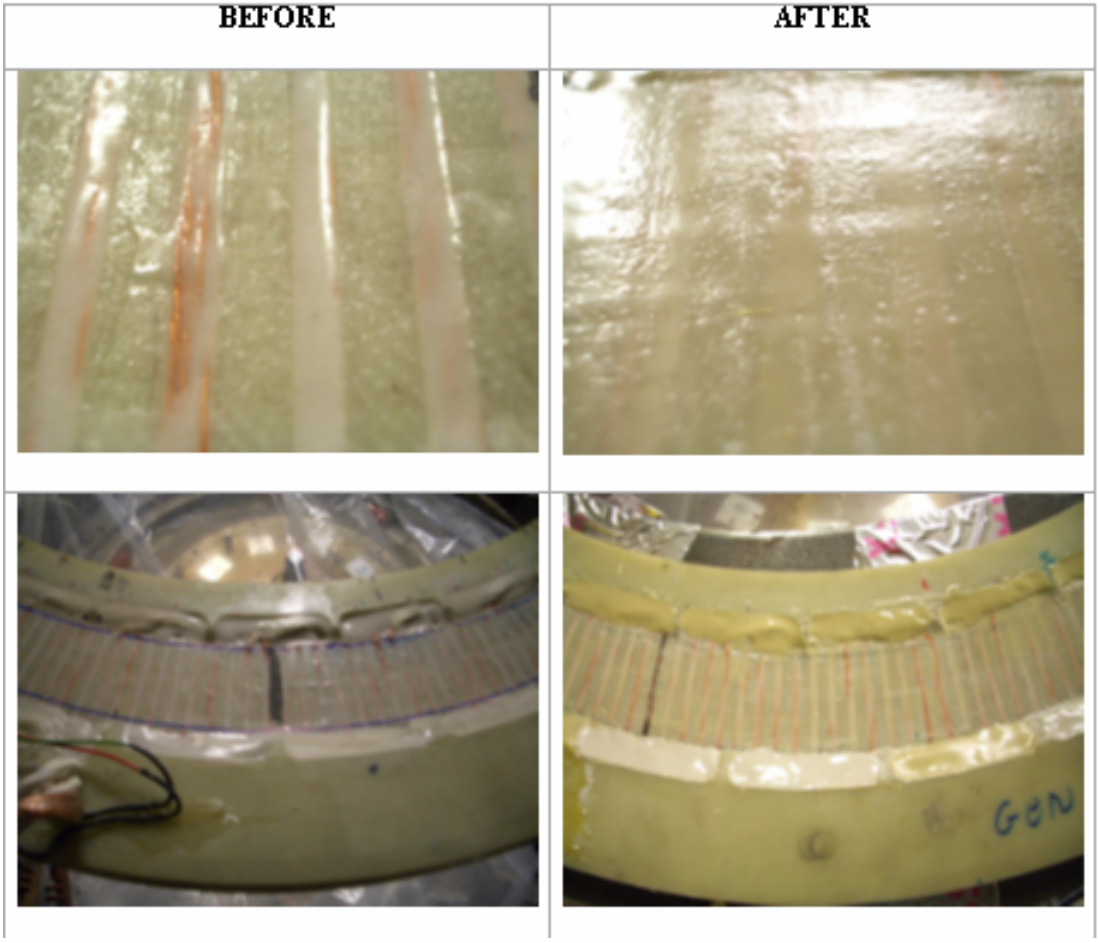

Fig. 56 Stator pictures before and after modifications

Yet another problem that was encountered was that when the circuit was closed, the current seemed to be limited. It increased gradually as the speed was increased but stopped increasing at about 20 A. It was suspected that the relay was not rated high enough and so must have burned out during previous testing. Research was done and it was discovered that the relay was not rated for much less than 150 A which was the current that was originally expected. For this reason, a two phase manual breaker, rated up to 200 A was installed into a large knife edge breaker box that was purchased as a

Fig. 57 Knife edge and breaker system

back up system. Longer wires were soldered to the motor-generator circuit ends so that they could be taken out of the rig, away from the pit area and into the breaker. The breaker's ground was connected to the building's ground by the black wire shown in the Fig. 57. A schematic for the circuit with the new breaker system is shown below:

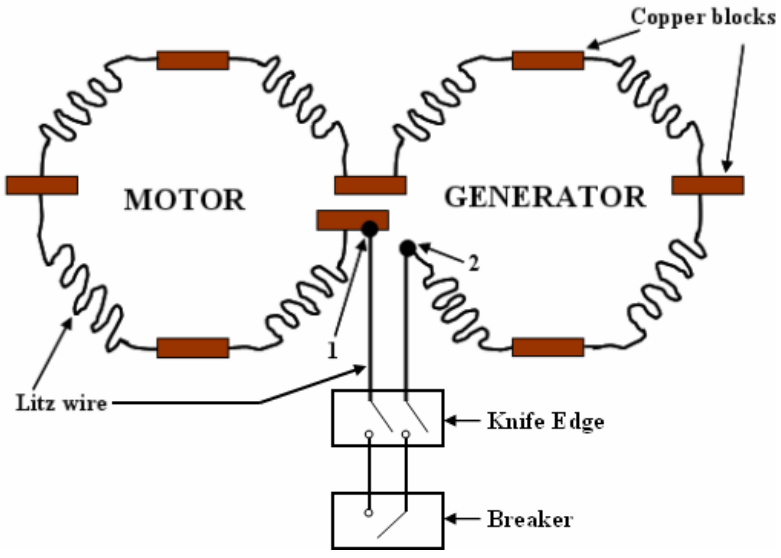

Fig. 58 Schematic for phase A wiring with new breaker system

As can be seen in the Fig. 58, the wires were connected across the knife edge breaker and then other wires were connected from the knife edge to the smaller breaker. Hence, during testing, the knife edge could be left in the closed position and the breaker could be used to open and close the circuit. The main purpose of the knife was to open the circuit in a case of emergency where the breaker could not open it.

Determination of Rotor – Stator Gaps

When the first set of tests was run, most of the data taken was obtained in open circuit. The open circuit voltage difference was used to determine the amount of current that would be expected when the circuit was closed. The expected current at the first target speed of 5000 rpm was larger than the 150 A current limit. As a result of this, the difference between the gaps had to be increased. One way to determine the new gaps is to use the required current to determine the required difference in magnetic flux density as shown in equations (2) and (3). This new flux difference could then be used with one known gap (and hence flux) to determine the other gap based on the linear relationship shown in equation (8). This method is however based solely on predictions and so was not used. Another way to determine the new gaps, which is what was used, is to use the data collected at any speed, from tests with the old gaps. This could be done by first acquiring projected motor and generator voltage, voltage difference, and expected current values at the speed where the new current is required. This projection can be made quite easily from old data since all of these variables should increase linearly with speed. Hence, the projections could be made using:

$$projected\_\text{var}iable = \frac{actual\_\text{var}iable}{actual\_speed} * projection\_speed \tag{61}$$

The ratio of the old voltage difference to the required voltage difference at the projected speed could then be determined and could be set equal to the ratio of old flux difference to new flux difference. That is:

$$\frac{Vdiff\_projected}{Vdiff\_required} = \frac{Bdiff\_old}{Bdiff\_new} \tag{62}$$

This is true because:

$$Vdiff = (BvL)gen - (BvL)motor = vL(Bgen - Bmot) = vLBdiff \tag{63}$$

$$\frac{Vdiff\_old}{Vdiff\_new} = \frac{vLBdiff\_old}{vLBdiff\_new} = \frac{Bdiff\_old}{Bdiff\_new} \tag{64}$$

The last step is carried out knowing that the length, *L*, and the speed, v, are the same in the numerator and denominator. With this, the new flux difference could then be determined. Hence if either of the motor or generator gap is known, it can be used to determine the flux using (8). This flux can then be used, with the flux difference determined from (62), to calculate the unknown flux. This flux could then be used to determine the size of the new gap. The new rotor – stator gaps were 0.07 in (70 mils) per side for the generator and 0.0865 in (86.5 mils) for the motor.

Testing was done after the gaps had been changed and all other modifications completed.

Results

Testing was primarily done to measure, record and analyze the open and closed circuit voltages, currents, and power outputs of the motor. Temperatures of the stators were also monitored during the testing. Modifications were made for the electrical as well as the thermal aspects and results after these modifications were recorded.

A typical open circuit generator and motor voltage versus time plot, in this case, at 1000rpm is shown in Fig. 59. The height difference between the two lines represents

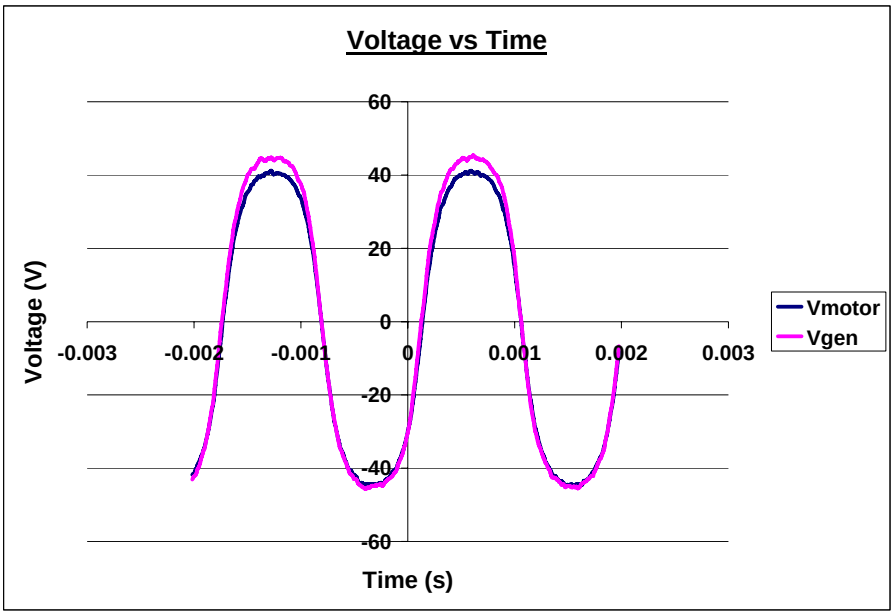

Fig. 59 Open circuit voltage waveforms

the difference between the motor and generator voltages. This voltage difference was determined by subtracting the plots and is shown in Fig. 60. The voltage difference was used to predict the output current and hence, power. Similar plots were made for 2000, 3000 and 3700rpm, the highest speed reached at the time. These plots were used to

determine root mean square (RMS) values for the voltage difference, which was then used to predict the expected RMS current and power outputs per phase. A straight line fit of the voltage difference data was used to get projected values for the voltage difference and hence expected current and power outputs at the 5000rpm target speed. All of this data is shown in Table 7. As can be seen in the table, the expected current at 5000rpm is much larger than the maximum allowable current of 150A. As a result, the difference between the motor and generator gaps was changed in an attempt to ensure a

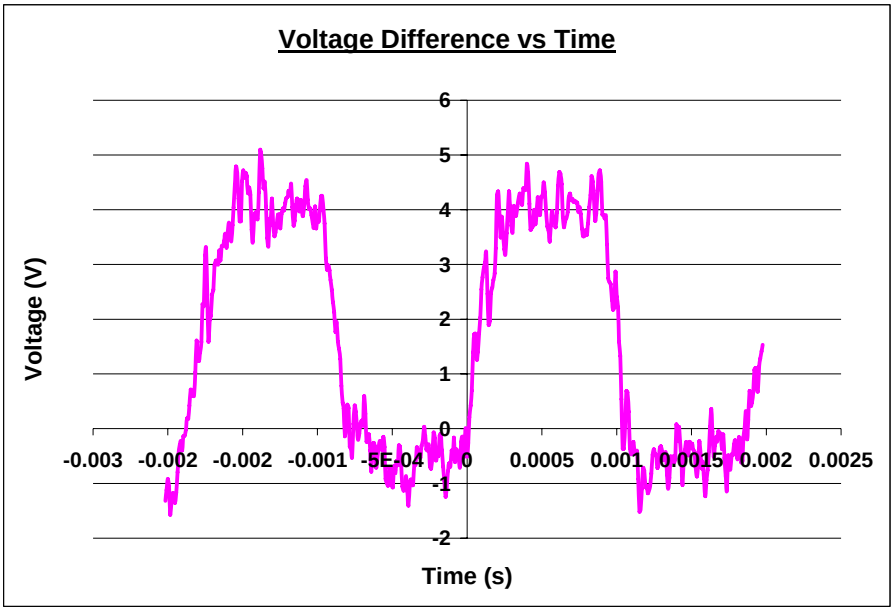

Fig. 60 Voltage difference waveform

current below 150A at 5000 rpm. The individual motor and generator gaps were also increased.

Table 7 Original open circuit motor data

Speed (rpm)	Motor Voltage (V)	Generator Voltage (V)	Voltage Difference (V)	Expected Current (A)	Expected Power (W)
1000	30.40	32.21	2.36	36.27	1193.88
2000	60.84	63.83	3.86	64.36	3915.64
3000	90.44	95.75	6.30	104.96	9492.64
3700	110.44	116.66	8.23	137.10	15140.35
5000 (projected)	151.00	159.5	10.50	175.00	26425.00

The open circuit motor and generator voltages were recorded with the new gaps. The same operations were carried out for this data to evaluate the expected current and power outputs per phase. These are shown in Table 8. As can be seen from Tables 7

Table 8 Open circuit motor data with new gaps

Speed (rpm)	Motor Voltage (V)	Generator Voltage (V)	Voltage Difference (V)	Expected Current (A)	Expected Power (W)
1000	27.85	28.54	1.18	19.70	548.64
2000	55.28	56.77	2.67	44.47	2458.39
3000	85.21	87.89	3.92	65.37	5569.99
4000	110.43	113.86	5.02	83.60	9232.05
5000	136.94	141.90	6.50	108.33	15112.50

and 8, the expected currents are much smaller with the new larger gaps and the expected current at 5000 rpm is smaller than the 150 A limit. With these new gaps, the motor was run up to 5000 rpm and the motor and generator voltages and their difference were recorded and used to determine the expected current and power outputs per phase. These values were plotted and are shown in Figs. 61, 62, and 63.

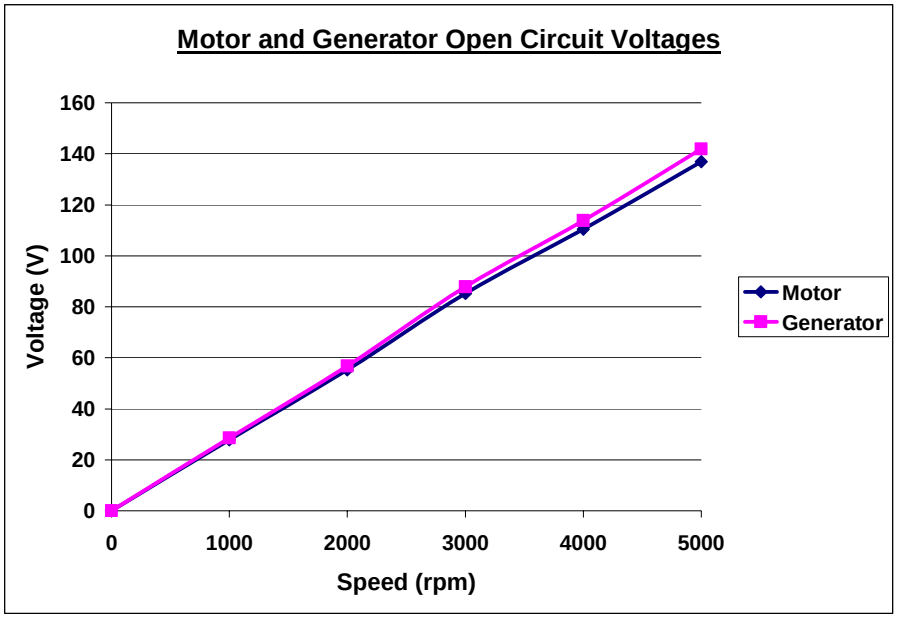

Fig. 61 Open circuit voltages from 0 - 5000 rpm

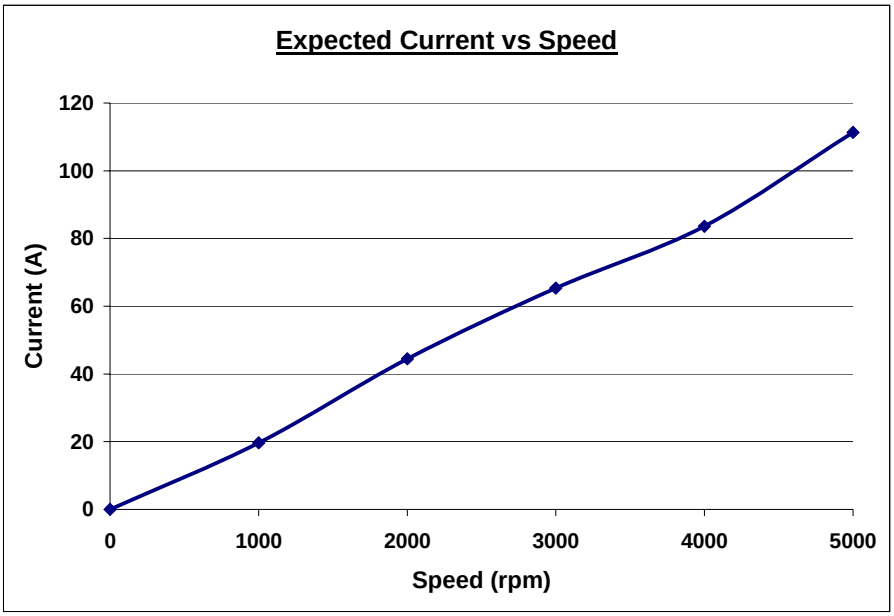

Fig. 62 Expected current from 0 - 5000 rpm

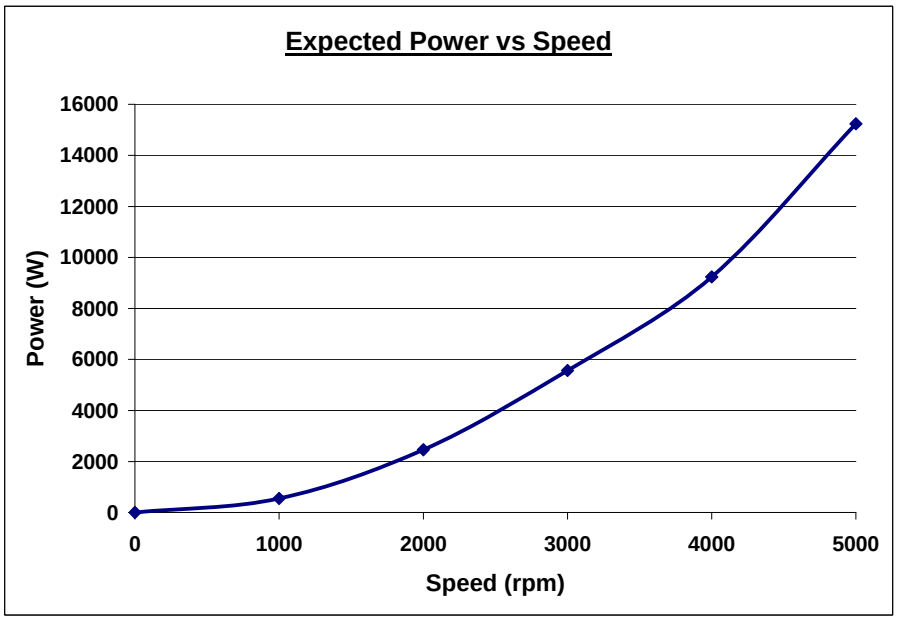

Fig. 63 Expected power outputs per phase

Closed circuit data was recorded during the testing when the breaker was flipped to its 'on' position to connect the motor and the generator. The closed circuit motor and generator voltages, and the current were measured and recorded. The motor and generator voltage waveforms are similar to the open circuit waveform shown in Fig. 59. A typical current waveform, in this case at 1000 rpm is shown in Fig. 64. The power output was evaluated from the motor voltage and current using:

$$P = iV\cos\varphi \tag{65}$$

where i is the current, V the voltage, P the power and φ the phase difference between the voltage and current waveforms. This phase difference, in degrees, was determined as follows:

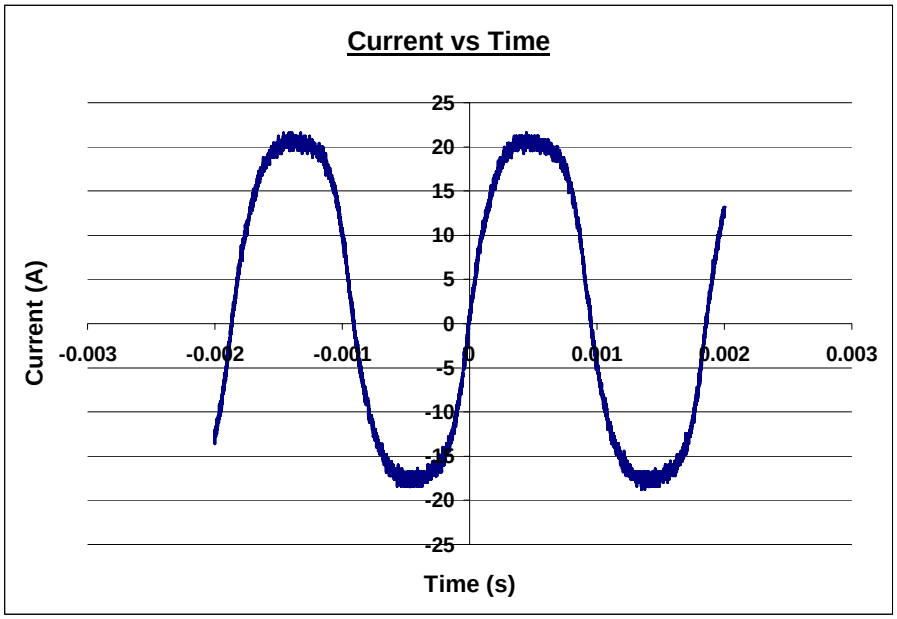

Fig. 64 Closed circuit current waveform

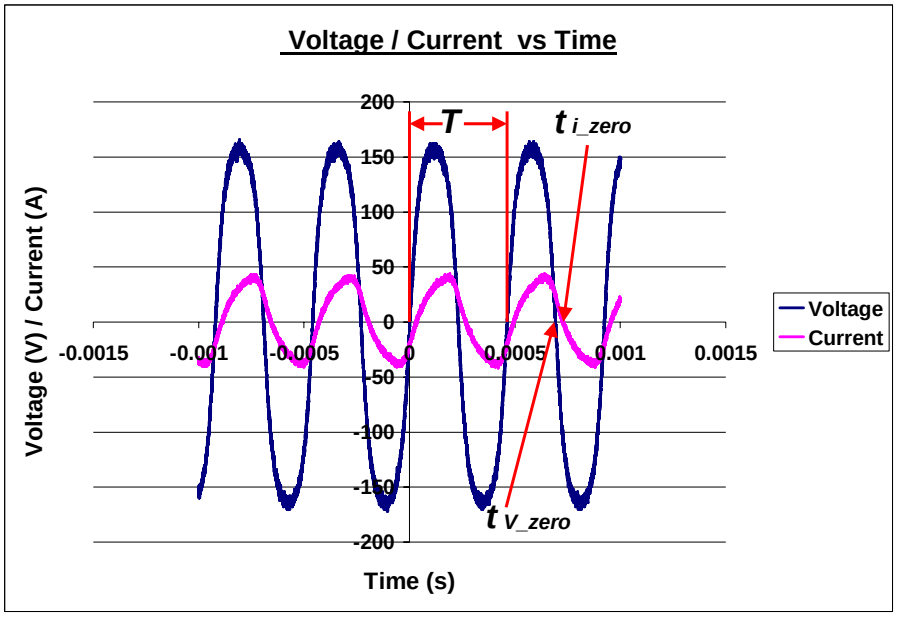

Fig. 65 Phase difference between current and voltage

$$\varphi = \left(\frac{t_{i\_zero} - t_{V\_zero}}{T} \right) * 360° \tag{66}$$

where t_{i_zero} and t_{V_zero} are the zero crossing times of the current and voltage waveforms respectively, and T is the period of the waveforms. These are shown in the Fig. 65. The iV term in equation (65) will be referred to as the peak power and the cosine term is called the power factor and will be used when the efficiency of the motor is to be determined. The closed circuit motor voltages, generator voltages, voltage differences, currents and peak power outputs per phase are shown in Table 9. As can be seen from the table, the measured current is much less than the expected current. It was suspected that this was due to a resistance and / or reactance in the rig that was causing a voltage drop across it and hence allowing less voltage to be put into current. Also, Table 9

Table 9 Closed circuit motor data

Speed (rpm)	Motor Voltage (V)	Generator Voltage (V)	Voltage Difference (V)	Current (A)	Peak Power per phase (W)
1000	32.10	32.7	0.51	8.49	281.71
2000	65.20	66.2	1.04	12.80	879.27
3000	99.80	101.6	1.52	14.85	1554.72
4000	136.00	138.5	2.07	16.97	2431.88
5000	173.90	177.5	2.67	17.68	3723.90

shows that there is a voltage difference in the closed circuit. When the circuit is closed, there should not be a voltage difference in the circuit. The presence of this voltage difference meant that there was a voltage drop between the points across which this voltage difference was measured. These points represent the point where litz wires were soldered to the wire ends from the motor and generator, shown as points 1 and 2 in the Fig. 58. These litz wires, a total length of about 10 meters, were brought out of the rig and into the knife edge to allow the circuit to be closed when necessary. Since the litz wire and the breaker were the only two parts present between the points across which the voltage difference was measured, it was certain that one or both of them were responsible for the voltage drop. To investigate this, the circuit was closed by soldering the wire ends together, thus bypassing the knife edge and breaker. The results from running the motor with this new configuration are shown in Table 10. As can be seen

Table 10 Closed circuit data without breaker

Speed (rpm)	Voltage Difference (V)	Current (A)	Peak Power per phase (W)
1000	0.45	10.39	333.66
2000	0.89	15.70	1023.49
3000	1.35	18.67	1863.03
4000	1.80	19.90	2702.28
5000	2.25	20.51	3566.01

from the table, the current is slightly larger and the voltage difference slightly smaller. This shows that the breaker was responsible for a little but not nearly the entire voltage drop measured. This left the litz wire as the only other possibility. Litz wire is generally known to not have high AC reactance but since they were the only parts remaining between the two points across which the voltage difference was measured, it seemed almost certain that they were responsible for the voltage drop. To investigate this, the litz wires coming from the points, were shortened by about 8 meters and rejoined to close the circuit. The motor was run again with this new configuration and the results are shown in Table 11. The table shows that the current increased by about 42 percent with this new configuration, and that the voltage difference, even though still present is substantially smaller. That means that this remaining voltage difference can probably be accounted for by the short litz wire that is still present between the points. The motor

Table 11 Closed circuit data with shorter wires

Speed (rpm)	Voltage Difference (V)	Current (A)	Peak Power per phase(W)
1000	0.14	15.34	492.55
2000	0.30	23.26	1516.80
3000	0.48	27.01	2695.75
4000	0.65	28.78	3913.98
5000	0.82	29.06	5053.89

and generator voltage stayed the same in all of these tests, which is why they are not included in Tables 9 and 10. Plots of the motor and generator closed circuit voltages, currents, and peak power outputs per phase with and without the breaker, and with the shorter wires are shown in Figs. 66, 67 and 68.

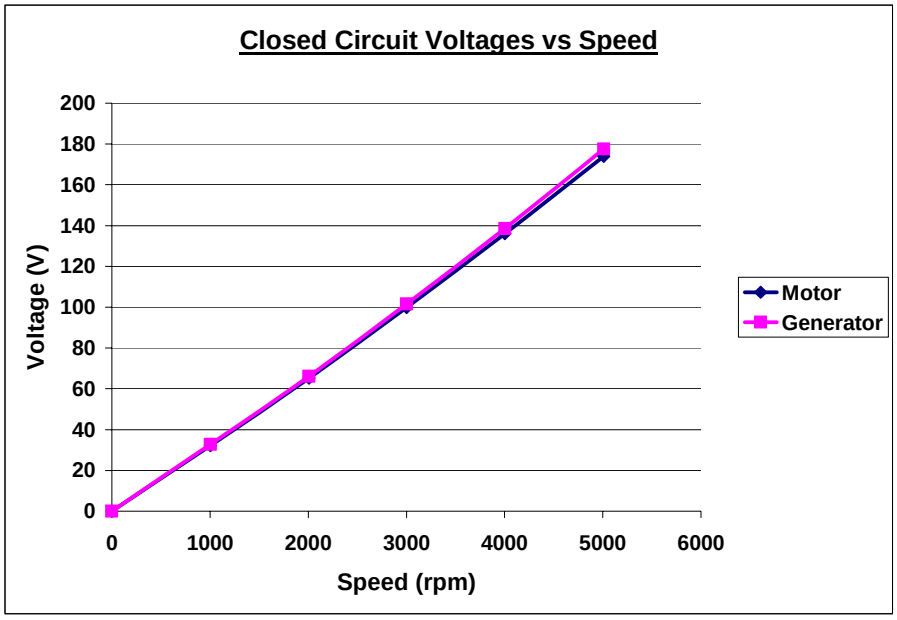

Fig. 66 Closed circuit voltages

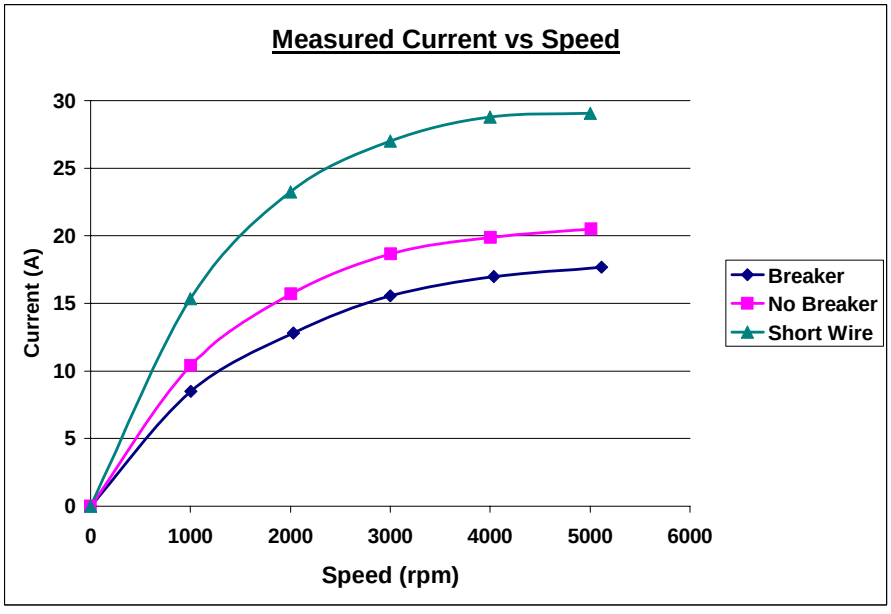

Fig. 67 Measured current

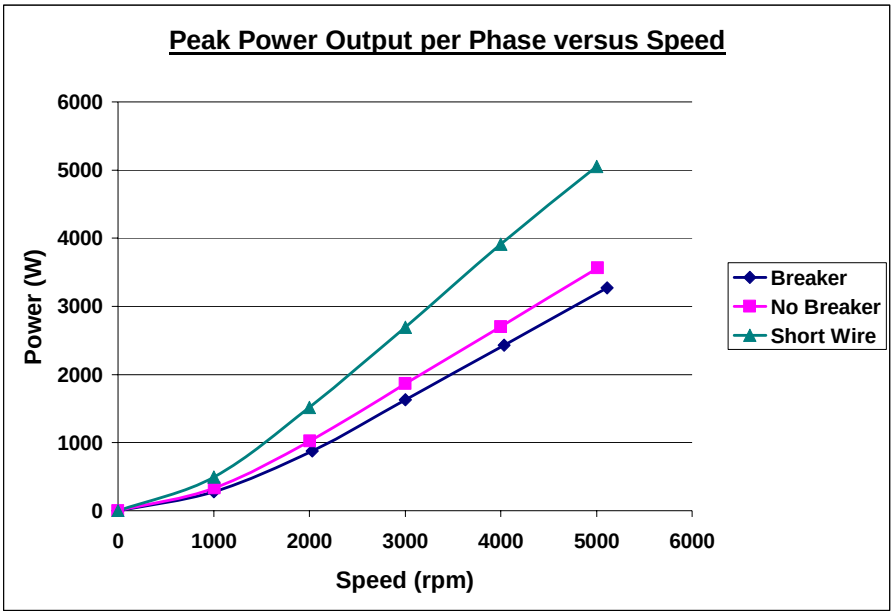

Fig. 68 Peak power outputs per phase

In determining the actual power produced by the motor, the power factor, described in equation (65) has to be used. The equation shows that optimum power production, and hence maximum efficiency would occur when the voltage and current waveforms are in phase, or when the φ term in the power factor is zero. The phase was monitored during testing and it was found that the phase difference was actually changing with speed. The phase difference was recorded with speed and plotted. As shown in Fig. 69, the phase difference between the motor voltage and the current appears to be changing almost linearly with speed.

As explained earlier, during closed circuit operation, the rig is self supporting, with the generator providing the current to drive the test motor and the test motor in turn producing torque to drive the generator. In a totally efficient system with no losses, the

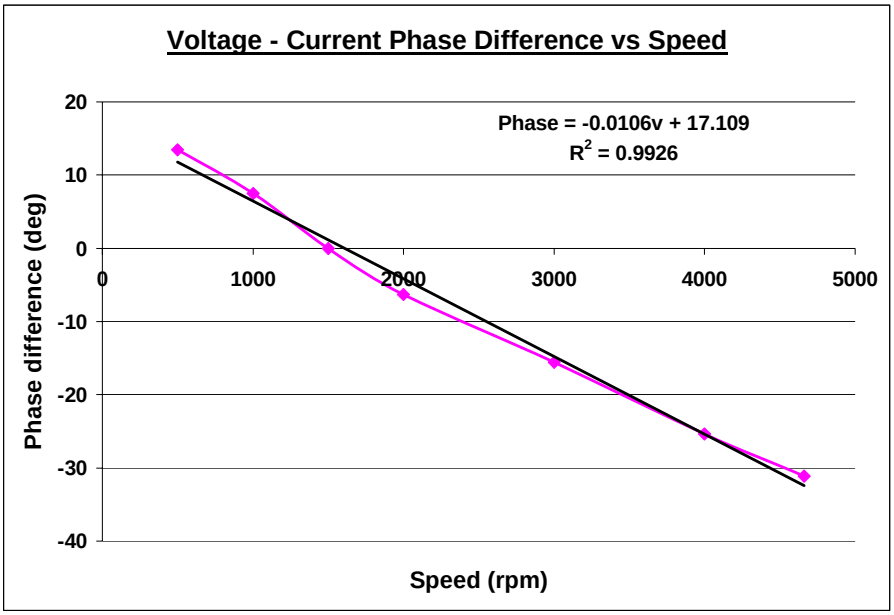

Fig. 69 Voltage - current phase difference versus speed

motor and generator when held at some speed would keep spinning at that speed. However, there are losses that make this impossible. When in closed circuit, the losses are compensated for by the auxiliary motor and so this enables the system to be held at a constant speed. When at a constant speed, the power provided by the auxiliary motor represent the losses at that speed and so can be used to evaluate the efficiency of the motor. A test was run to evaluate the efficiency of the system and the required data from this test was recorded. Prior to the test, the phase angle was set to be zero at 1500 rpm to make it represent the peak efficiency speed. The data from this test was recorded and is shown in Table 12.

The temperature of the stator was also monitored during testing since it increased rapidly as the speed was increased. Modifications were made in an attempt to slow

Table 12 Data for evaluation of efficiency

Speed (rpm)	Current (A)	Voltage (V)	[Phase] (degrees)	Aux. Motor Out. Current (A)	Aux Motor Out. Voltage (V)
1000	17.5	31.0	7.5	9.1	44
1500	21.7	46.7	0	10.5	66
2000	24.7	62.6	6.33	12.1	88.2
3000	27.6	97.1	15.54	17.4	135.8
4000	28.0	126.0	25.37	23.4	181

down the rate of the stator's temperature increase. The stator temperature was plotted against speed and time before and after the modifications. The plots before and after the first set of modifications were compared. In order to compare the temperatures accurately, the rate of speed increase after the modifications was carried out, carefully following the rates before the modifications so that the same speeds could be reached at about the same times. A plot of speed versus time showing the similar rates of speed increase is shown in Fig. 70. Plots of temperature versus time and speed before and after the first set of modifications are shown in Figs. 71 and 72. The great change in the slopes of the temperature versus speed plots at about 3500 rpm (Fig. 72) is due to the fact that the speed was increased much more slowly after this point as can be seen from the speed versus time plot. This decrease in the rate of speed was because the auxiliary motor that was used when the data before the modifications was taken was not quite

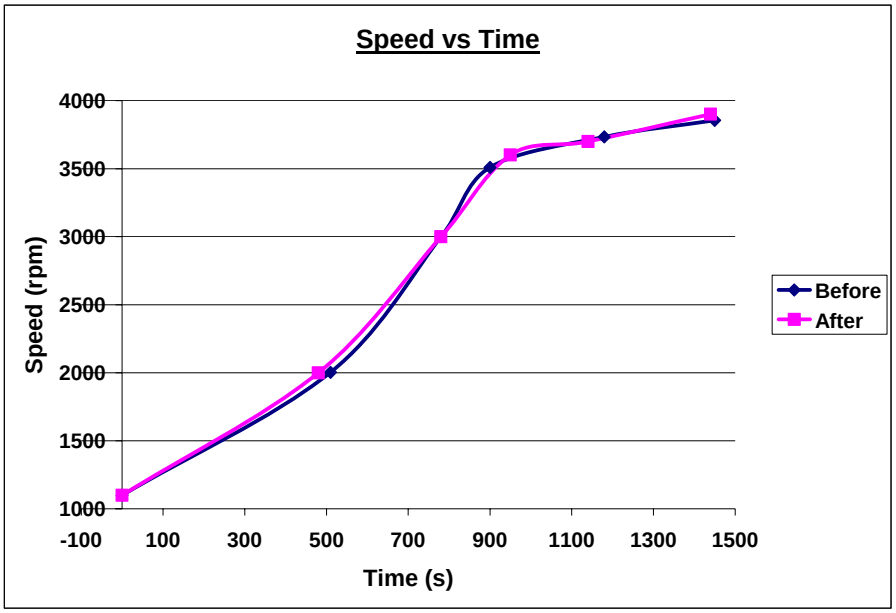

Fig. 70 Speed comparison after first modification

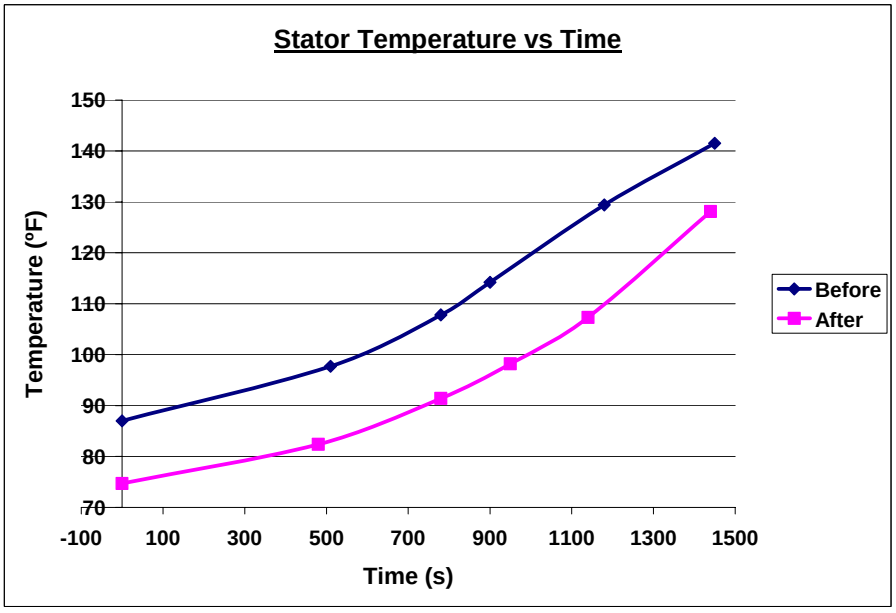

Fig. 71 Temperature-time comparison after first modification

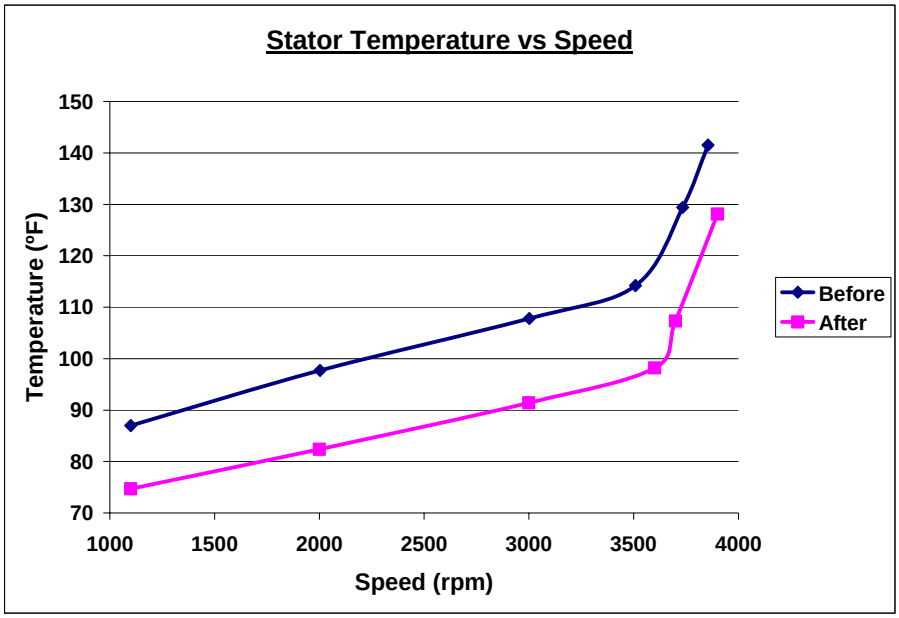

Fig. 72 Temperature-speed comparison after first modification

powerful enough and so struggled to increase the speed after this point. This had to be repeated for the data after the modifications, even though the auxiliary motor was more powerful, so that the results could be compared. As can be seen from the plots, even though the temperatures appear to be lower at each speed, the rate of temperature increase is about the same. The same plots were made after the holes were drilled in the magnetic discs, this time, comparing it to the results after the first set of modifications. The plots are shown in Figs.73, 74, and 75. As can be seen from the plots, the stator temperature increased more rapidly without the holes than it did with the holes.

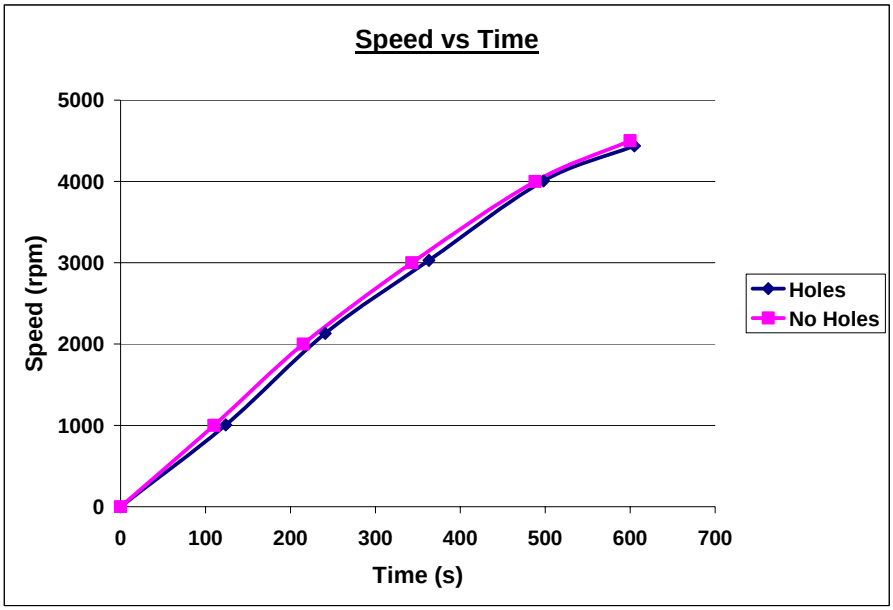

Fig. 73 Speed comparison with and without holes

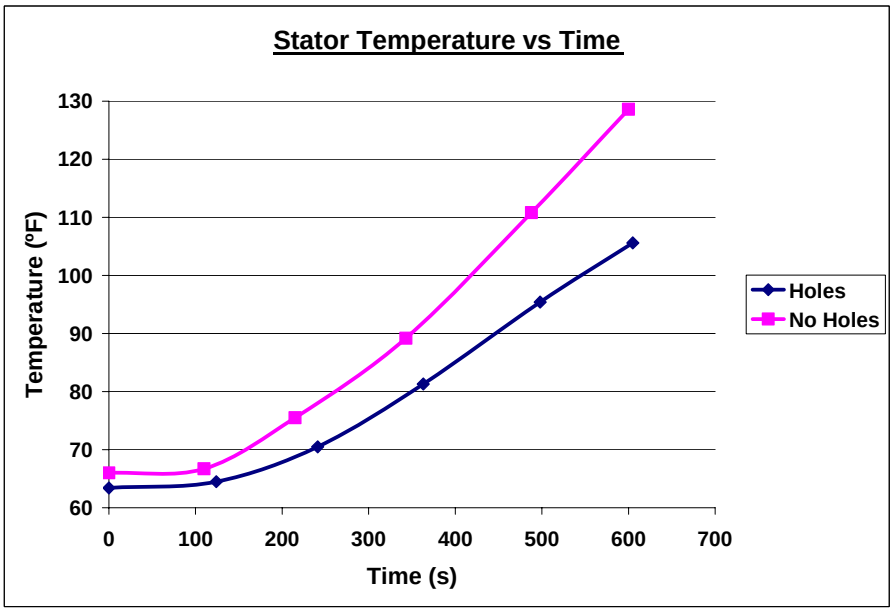

Fig. 74 Temperature-time comparison with and without holes

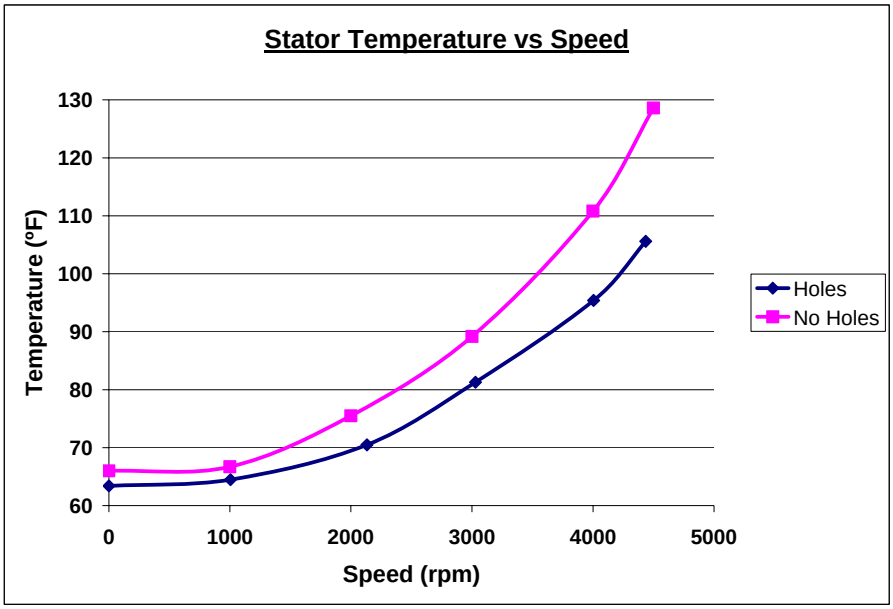

Fig. 75 Temperature-speed comparison with and without holes

The power losses (windage, bearing, etc.) from the motor were also assessed during testing. This was done by driving the motor up to a high speed and recording the speed and time as it coasted down to a stop. The speed was then used to determine the kinetic energy at each speed using:

$$E = \frac{1}{2} I \omega^2 \tag{67}$$

where E is the kinetic energy, I the moment of inertia and ω the angular velocity. This energy was plotted as a function of time and the curve was differentiated with respect to time to determine the power losses. The differentiation was carried out by breaking the curve into small portions, getting the polynomial curved fit of each portion, and then differentiating the polynomial equations to get approximate power equations. An example of the energy versus time curve, broken down into seven portions and curve

fitted, showing the curve fit equations and goodness of fit parameter (R^2) values is shown in Fig. 76. These equations were then used to approximate the power losses at

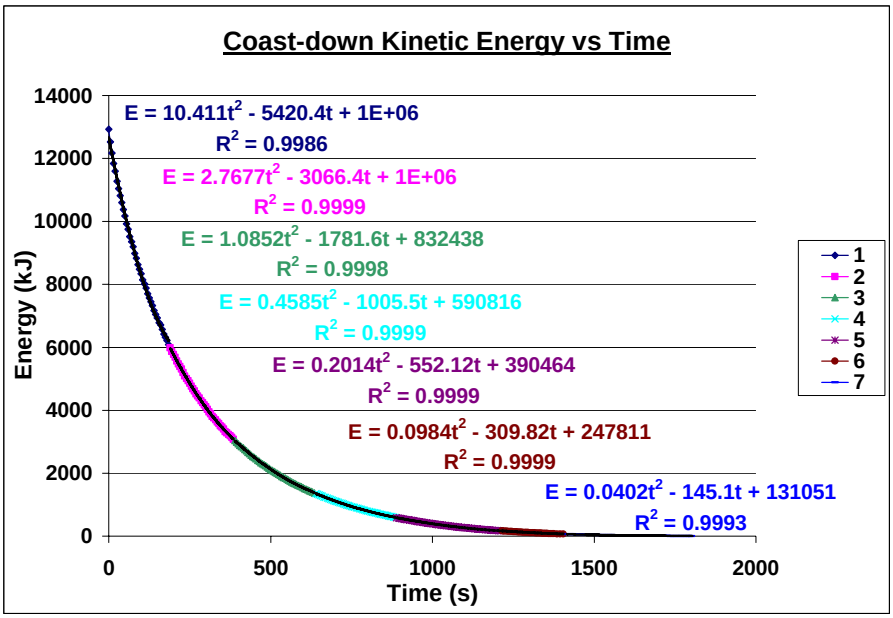

Fig. 76 Sample segmented coast-down kinetic energy plot

each speed and these power losses were plotted against time.

The determination of power losses during coast-down, discussed above, was carried out before and after the modifications. Hence, it was carried out with the original gaps and initial rough stator surface conditions, and again with the new gaps and smoother stator surface. Plots of speed versus time, and the corresponding power loss versus speed during the coast-down are show in Figs. 77 and 78. A polynomial curve fit was made for the power – speed relationship and the corresponding equations and goodness of fit parameter (R^2) are shown in Fig. 78. This was done in case predictions were to be made for the losses at higher speeds.

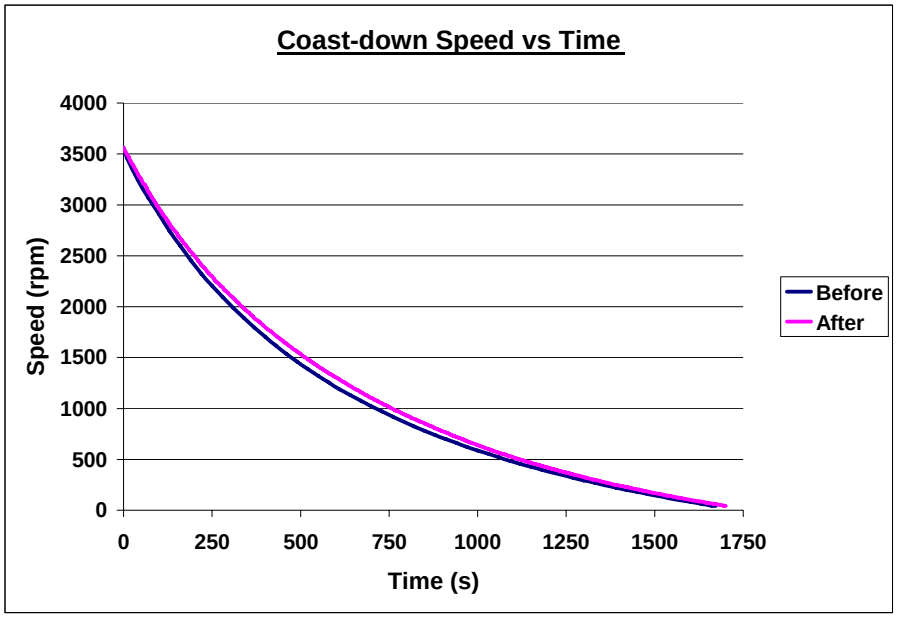

Fig. 77 Coast-down speed versus time before and after modifications

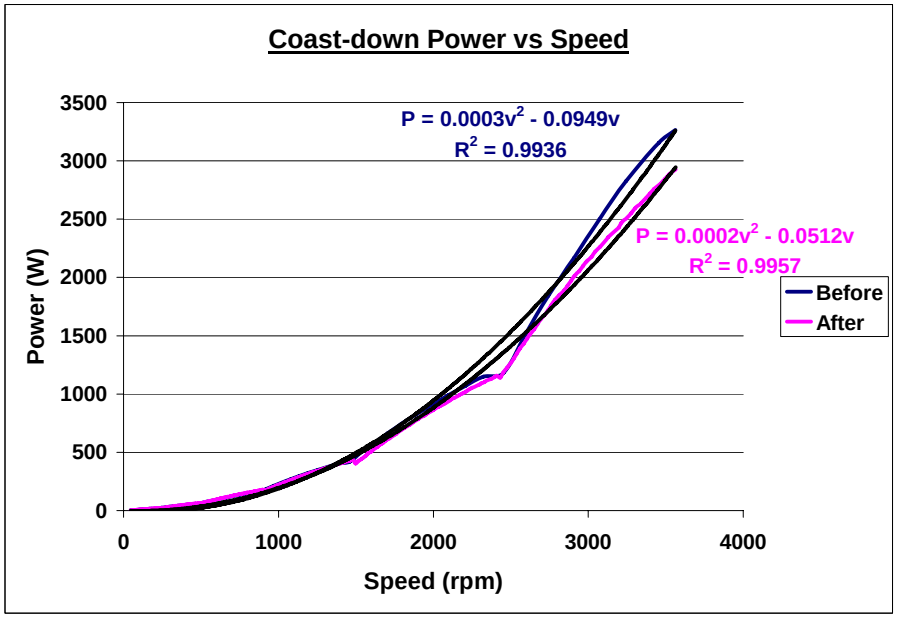

Fig. 78 Coast-down power versus speed before and after modifications

Discussion of Results

The majority of the results recorded during testing are in line with what was expected. The open circuit voltages are almost exactly the same as what was predicted in the model. The predictions were made using the initial magnet – stator gaps of 35 mils for the generator and 59 mils for the motor. The results recorded with these initial gaps are compared to the predictions in Figs.79 and 80. As can be seen from the plots, the

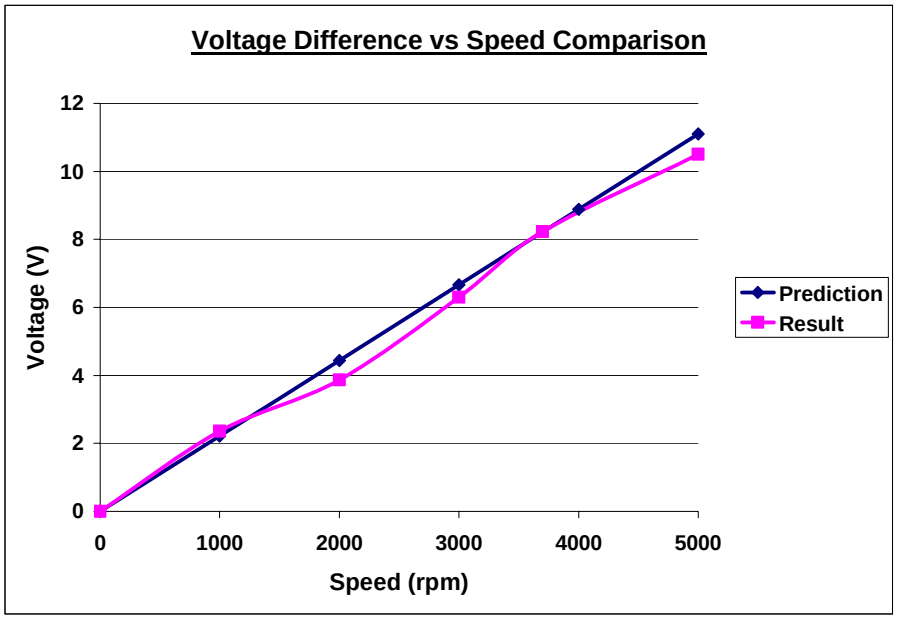

Fig. 79 Voltage difference comparison with predictions

results are quite accurate with the predictions. The slight differences are probably due to instrument error and slight losses in the system

The gap modifications made in the motor and generator to keep the expected current at 5000 rpm was successful. They reduced the voltage difference so that the expected current (Fig. 81) derived from this difference was acceptable. This reduction

was done at the expense of the expected output power since the power was predicted based on this expected current. This however was necessary to ensure that the stator did not warp from the current being above its limit, as this would lead to rubbing between the stator and the rotor, which would damage the rig and be very dangerous for people around the test area. The expected current and peak power reductions are shown in Figs. 81 and 82. All of this was done prior to obtaining the closed circuit data.

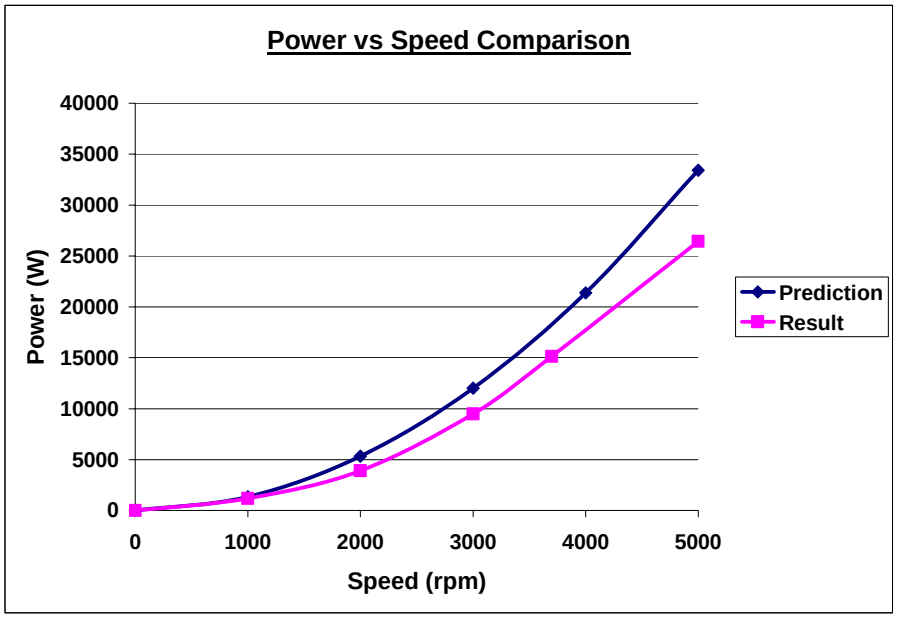

Fig. 80 Power comparison with predictions

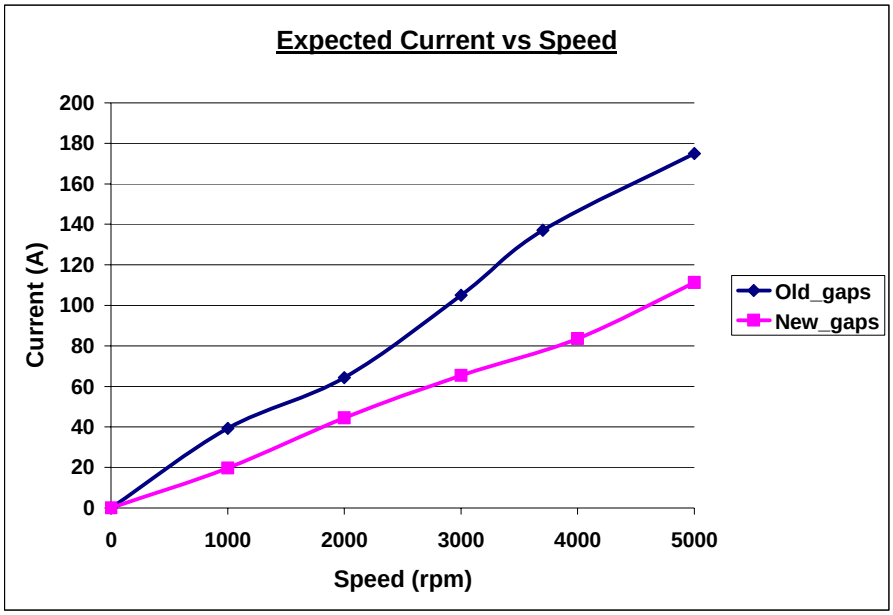

Fig. 81 Expected current before and after gap modifications

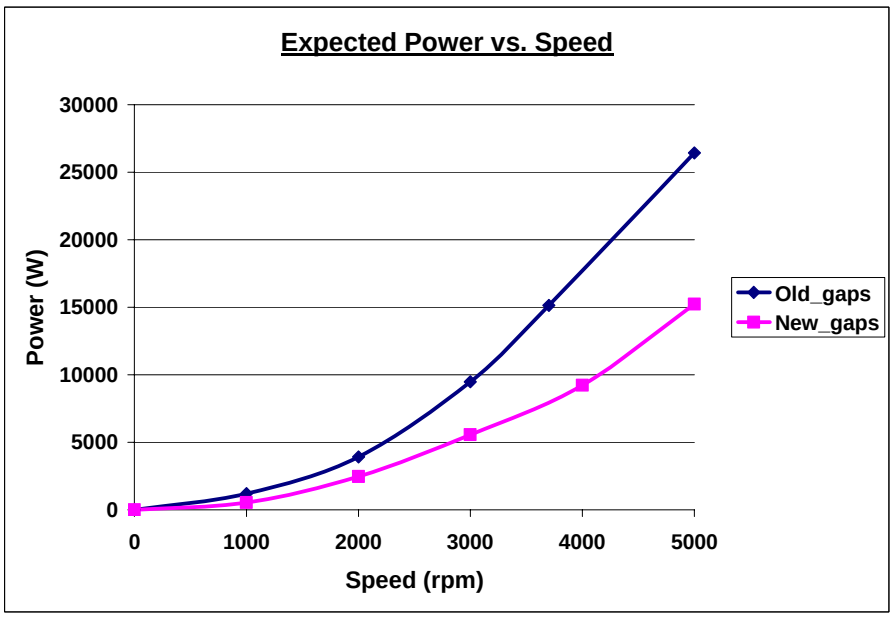

Fig. 82 Expected peak power output before and after gap modifications

The closed circuit data was quite different from what was expected. The motor and generator voltages were in line with the expectations since they were supposed to be almost the same as the open circuit voltages. However, as can be seen from Fig. 67 and Fig. 68, the measured current and peak power output per phase were very different. The measured currents were much smaller than the expected currents, which in turn meant that the peak power output per phase was much smaller. As was shown in the results, the current increased when the knife edge and breaker were eliminated, and increased even more when the wires were shortened. All of these were still much lower than the expected current which in turn meant that the peak power was much less than the expected peak power. The difference between the expected and measured values of

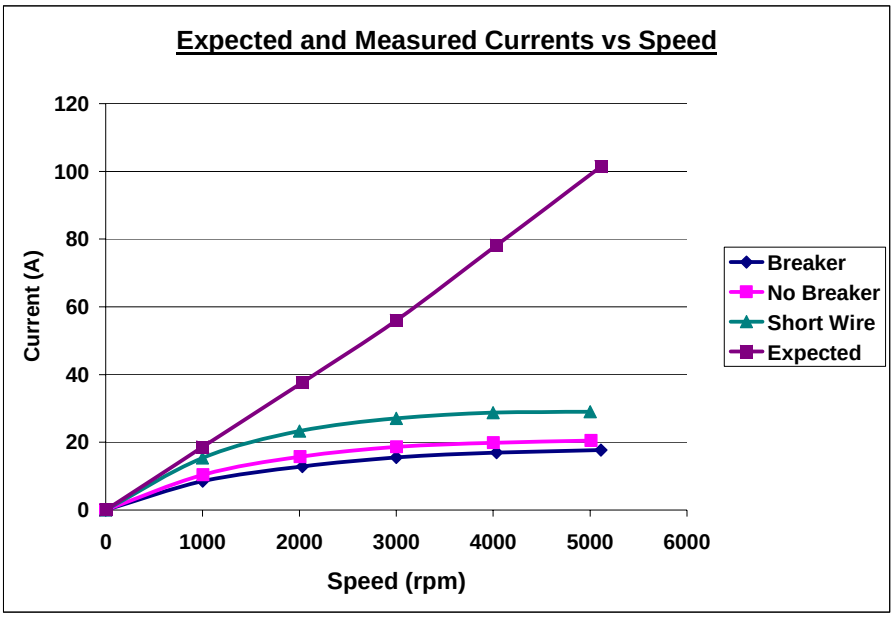

Fig. 83 Expected and measured currents

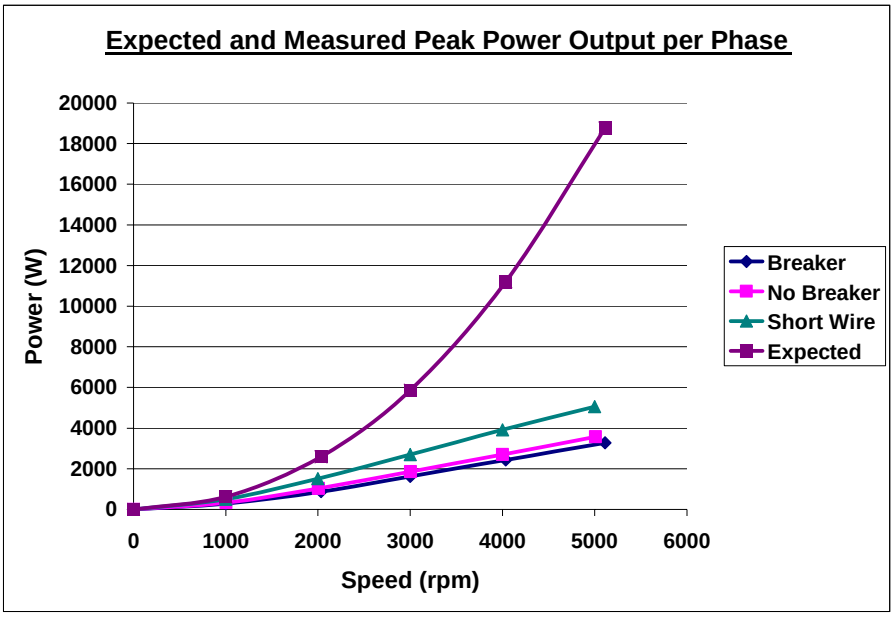

Fig. 84 Expected and measured peak power output per phase

the current and the peak power output per phase are shown in Figs. 83 and 84. The current and power were expected to increase linearly and quadratically respectively. However, the current saturates and the peak power increases linearly after 1000rpm. The current saturation at a value much smaller than what was expected implies that there is some reactance in the rig that is causing the current to saturate. Also, the fact that there is a voltage difference between points 1 and 2 in Fig. 85 shows that there is a total impedance between those points that is causing the voltage drop read. To investigate this, two impedance variables were evaluated: the total rig impedance was evaluated by dividing the open circuit voltage difference by the measured current, and the impedance between the points 1 and 2 was evaluated by dividing the measured closed loop voltage difference by the current. That is:

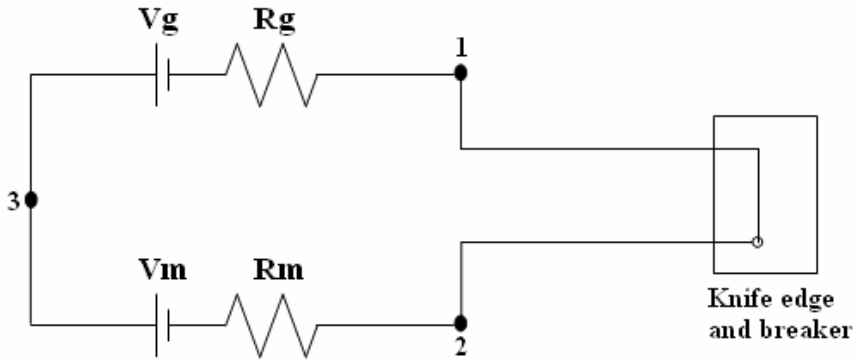

Fig. 85 Schematic for motor-generator

$$Z_{\_total} = \frac{O.V_{diff}}{i} \tag{68}$$

$$Z_{\_12} = \frac{C.V_{diff}}{i} \tag{69}$$

where Z is the impedance, 12 means across points 1 and 2, and the $O.$ and $C.$ are used to refer to open and closed circuit. The total impedance includes the resistance and reactance around the whole circuit: from 1 through 3 and 2 and back to 1. The open circuit voltage difference was used to evaluate this total impedance because that voltage difference represents the total voltage that should be used to produce current when the circuit is closed. The two impedance parameters were determined for each of the closed circuit tests. The impedances evaluated are shown in Tables 13 and 14. These values are plotted and shown in Fig. 86. As is shown in the plots, the impedances all seem to be increasing linearly with the speed. This would imply that the resistances and / or the reactances are increasing as the frequency increases. It was suspected that the copper blocks that connect the quadrants of the stator could be the cause of some of the high

Table 13 Total rig impedance

	Total Impedance (ohm)		
Speed (rpm)	**Breaker**	**No Breaker**	**Shorter Wire**
1000	0.132	0.107	0.073
2000	0.176	0.144	0.097
3000	0.226	0.180	0.124
4000	0.276	0.236	0.163
5000	0.344	0.296	0.209

Table 14 Impedance between motor - generator wire ends

	Impedance between points 1 and 2 (ohm)		
Speed (rpm)	**Breaker**	**No Breaker**	**Shorter Wire**
1000	0.061	0.044	0.009
2000	0.081	0.057	0.013
3000	0.103	0.072	0.018
4000	0.122	0.091	0.023
5000	0.151	0.109	0.028

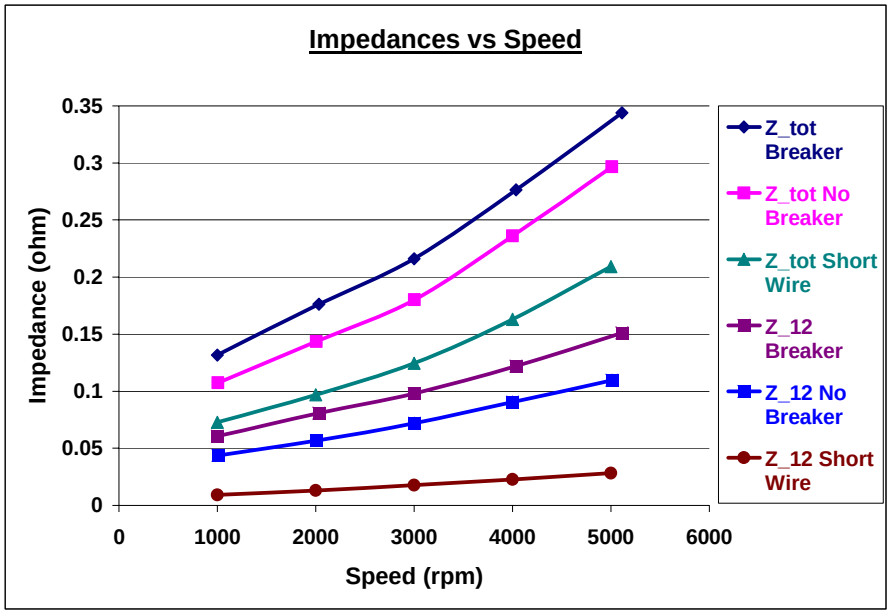

Fig. 86 Rig impedances versus speed

impedances present in the rig. To investigate this, a 'dummy' copper block was installed between 1 and 2 and used to close the circuit by soldering the litz wires to the ends of the copper blocks. When testing was done with this configuration the measured currents were the same as without the dummy blocks.. This meant that the copper blocks were not responsible for the frequency dependent reactances. It is strange that the wires could have these high impedances because litz wire is designed to have low AC resistances / reactance, also called skin depth. However, the litz wire does indeed have some reactances that are increasing with speed. This is obvious because as can be seen from the plots, when 8.12 m of the litz wire was removed from between points 1 and 2, the current increased by 42% and the impedance dropped by the large difference shown between the bottom two plots in Fig. 86. This is very significant considering the fact that there are a total of almost 30 mils of litz wire in the whole circuit. The presence of

these reactances is also confirmed by the fact that, as shown in the results, the phase difference was increasing with speed. This is important because the phase difference is normally related to the resistance and impedance (combination of resistance and reactance) by:

$$\cos\varphi = \frac{R}{Z} \tag{70}$$

or related to the total reactance by:

$$\tan\varphi = \frac{X_L - X_C}{R} \tag{71}$$

where R is the internal resistance, X_C is the capacitive reactance and X_L is the inductive reactance. Hence if the phase is changing in one direction or with one parameter, the reactance is likely to also change with that parameter and in that direction.

This reactance evaluated in the rig could be due to a few factors such as the skin effect, eddy currents and the presence of back emf. "The skin effect is the tendency of an alternating electric current to distribute itself within a conductor so that the current density near the surface of the conductor is greater than that at its core. Hence, the electric current tends to flow at the 'skin' of the conductor. The skin effect causes the effective resistance of the conductor to increase with the frequency of the current." [11] This skin depth is proportional to the inverse of the square root of the frequency and the effective resistance is inversely proportional to the skin depth. Litz wire is generally designed to be free of the skin effect unless at very high frequencies. The #38 litz wire used in the test motor is quoted as being able to handle frequencies of up to 50 KHz. Eddy currents could also increase the total reactance. This is not likely in the stranded

litz wires though since the small insulated cross sectional areas stop the currents from circulating within the cross-sectional area. However, research has shown that there could be eddy currents in the conductive permanent magnets. Amara et al. explain that some new 'modular' permanent magnet machines, in which the fundamental component of the stator magnetomotive force (MMF) has fewer poles than that of the permanent-magnet armature, can have significant eddy-current loss in the moving magnet armature They explain that these eddy currents are caused by the presence of lower and higher order space harmonics in the stator winding MMF distribution [12]. In other words, if the stator winding in the test motor imposes a change in flux, this will induce eddy currents on the rotating magnets which will induce a flux that opposes the original flux. This idea has not been severely entertained in this research but further research will be done to investigate the likelihood of such eddy currents in the test motor. The increase in the total reactance could also be due to the presence of a back emf in the circuit. This is possible because the torque produced by the motor could be opposing the magnetic field, thus causing the back emf. It is certain that there is a reactance in the rig and in the litz wires that is increasing with speed (and hence frequency) and is causing the current to saturate as the speed is increased. It is however uncertain what exactly is causing this increasing reactance or if it is a combination of various effects.

The results for the stator temperature were also compared to the predicted temperatures from the model, based on the same gap size. Plots of temperature versus speed for the model and for the actual test are shown in Fig. 87. As can be seen in the

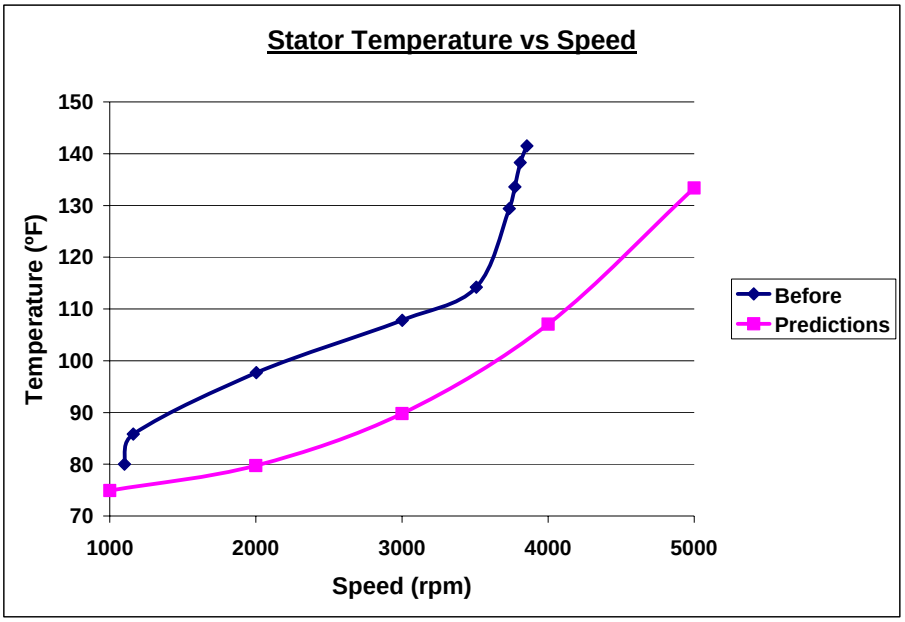

Fig. 87 Temperature comparison between predictions and results

the figure, the actual temperature results are much larger than the predicted results. This could be due to a few reasons such as the rotor temperature not being the same as the temperature of the rotor – stator gap air, as was assumed in the predictions. Also, the stator was probably heating up from reasons other than the windage power losses. Most importantly, the predictions were made assuming that the speed was increased linearly with time and that it took 600 seconds to go from 0 to 5000 rpm which was not the case in the tests. Now, looking at the results, the temperatures before and after the modifications was compared. As was stated in the results, although the temperatures after the first set of modifications appear much lower at each speed than they were before the modifications, the rate of increase of the temperatures, shown as the slopes of the plots, was still about the same. The temperature difference at each speed is present because the starting temperatures for both tests are different. The test before the

modifications was carried not too long after a previous test and so the stator temperatures had not gone back to room temperature. Hence, while the temperatures are lower, the change in temperatures between start and finish is almost the same. The differences were taken and show that in going from 0 to 3900 rpm in 24 minutes, the temperature increased by 54.6 ºF before and by 56.5 ºF after. The results after the holes were drilled are much different though. As is shown in the plots, the rate of temperature increase, shown as the slopes of the plots, was greater before the holes were drilled than after. The temperature change was also a lot smaller with the holes than without the holes: In going from 0 to 5000 rpm in 10 minutes, temperature increased by 62.6 ºF without the holes and by 42.2 ºF with the holes. The holes would have been more effective if they were bigger since they would allow more air to get into the gaps. However, there was very limited space on the magnetic discs due to the presence of the magnets.

The windage losses predicted using the moody friction factor are much smaller than the power losses evaluated during coast-down. This difference is probably due the fact that while the windage predictions were solely for the friction between the rotating magnets and the stator, the coast-down power losses include all losses including bearing, friction on all other parts of the rig, pulley and belt restrictions, drag forces, etc. The main factor that makes the coast down losses very large is probably the resistance provided by the belt from the auxiliary motor. Belts are made to conform to the pulley sizes but as the pulleys get smaller, the belts used become less willing to bend and thus provide a great resistance to the rotation. The tension in the belt also provides a

resistance force that opposes the rotation. Moreover, when the auxiliary motor control is turned off without the load coupled to it, it goes down to 0 rpm in a few seconds. Hence, it is logical to think that when it is turned off with the load, it will impart some resistance to the rotation of the test motor. Finally, comparing the effects of the windage modification data, it can clearly be seen from the plots that there is not that much of an improvement. There appears to be a slight difference in the coast-down power plots but it is not substantial. This is in line with the model predictions that increasing the gap does not substantially reduce the windage losses. The coast down method appears to be a good indication of the total losses from the rig. As is shown in Fig. 88, the power plots

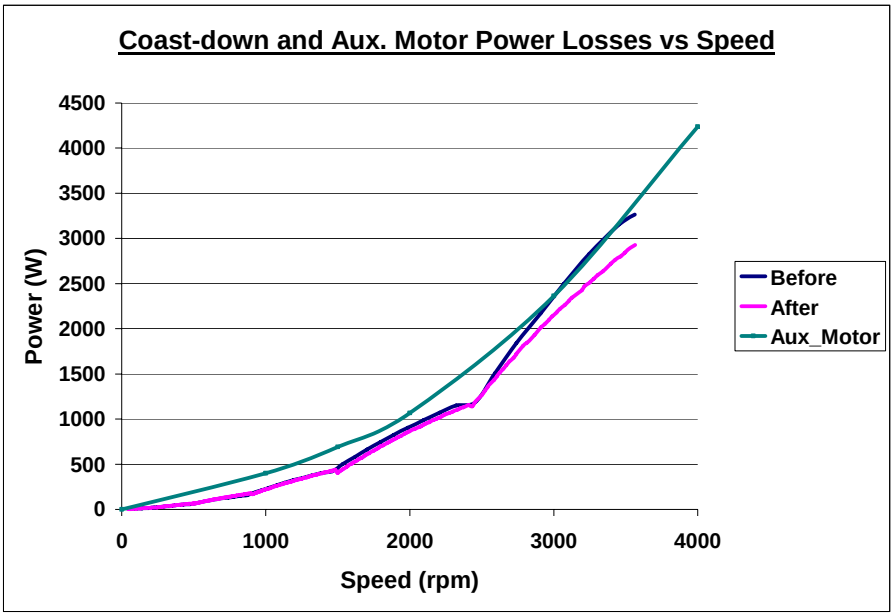

Fig. 88 Power loss comparison between coast down and auxiliary motor

evaluated from the coast down run are quite similar to the losses reflected by the auxiliary motor.

Finally, the efficiency of the test motor was evaluated based on the data given in Table 12. It was evaluated using the following equation:

$$Efficiency = \left(1 - \frac{P_{losses}}{P_{output}}\right) * 100 \tag{72}$$

where P_{losses} represents the total losses from the system and P_{output} represents the total power produced from all four phases. Since the phase changes as the speed is increased, the efficiency was different at each speed. As was stated in the results, the phase angle was set to zero degrees at 1500 rpm, making it the top efficiency speed for that test. P_{losses} is the power output of the auxiliary motor and was evaluated by taking the product of the auxiliary motor's output current and output voltage. That is:

$$P_{losses} = \left(i_{output} * V_{output}\right)_{AUX.MOTOR} \tag{73}$$

Since all the phases are exactly identical, P_{output} can be evaluated as four times the power produced from phase A, the only phase whose circuit was actually closed. Therefore, the power output is:

$$P_{output} = 4 * iV\cos\varphi \tag{74}$$

The outputs and losses were evaluated at each speed and were used to evaluate the efficiency at each speed. Values for the total power loss, total power output for all phases and efficiency of the motor are shown in Table 15. A plot of efficiency versus speed is shown in Fig. 89.

Table 15 Evaluation of efficiency

Speed (rpm)	P_{losses} (W)	P_{output} (W)	Efficiency (%)
1000	400.40	2151.44	81.39
1500	693.00	4053.56	82.90
2000	1067.22	6147.17	82.64
3000	2362.92	10327.96	77.12
4000	4235.4	12620.51	66.78

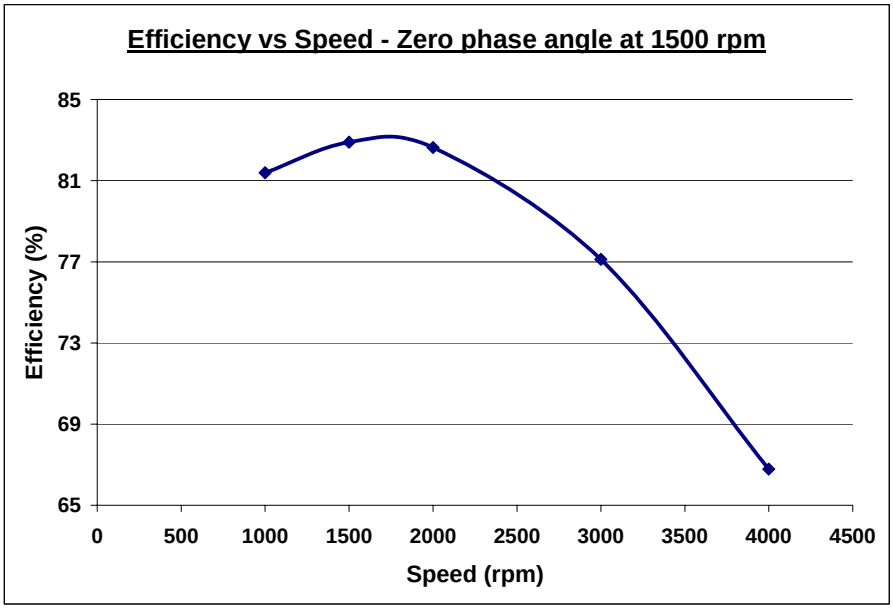

Fig. 89 Efficiency for 1000 – 4000 rpm

SUMMARY AND CONCLUSIONS

Summary

This need to design a high power density motor has been met with NASA's design of this test motor. The test motor has been run and has demonstrated that it does not require a dynamometer to provide the torque to spin it. The main variables have been researched and results have been acquired. Modifications were made based on these results in an attempt to improve the operation of the motor. Most of the results were successful and the ones that did not yield the expected results have been studied, noting the reasons why they were not effective.

The electric quantities, voltages, currents, and power, measured in this research have been plotted and studied. An analysis directly relating the rotor - stator gap sizes and their difference to these electrical variables, based on previously collected data, has been carried out. The motor output voltage turned out almost exactly as expected and increased linearly with the speed. The current, expected to also increase linearly reached a saturation value above which it did not increase further. The power, expected to increase quadratically increases linearly after 1000 rpm even after a few changes were made to increase the saturation value of the current by a total of about 64 percent. The saturation value of the current was much lower than what was expected based on the total voltage available to the circuit, revealing the presence of alternating current reactance in the rig that grows with speed (and hence frequency). The #38 litz wire, expected to have very low AC resistance and reactance, does have some reactance that

increases with frequency. The presence of this reactance causes the phase difference between the output current and voltages to increase with frequency, which means that the efficiency of the system changes with the speed. The phase of the system can be adjusted which means that a speed can be predefined as the maximum efficiency speed. With the tests that were carried out, it appears that the AC reactance in the wires cannot be fully eliminated. This means that even though the current can be increased, it is always going to saturate, which in turn means that the power is always going to become a linear function of speed.

The tests have shown that there is a considerable amount of heat energy going into the stator due to the magnetic discs rotating over them with very small gaps. It has been predetermined that the wires within the stator start expanding at 155 ºF. This means that with the current stator configuration, the expansion of the wires will cause the stator to bend downwards, thereby contacting the rotating magnets. This made it very important to keep the stator temperatures below 155 ºF. While more work needs to be done to get the stator temperature even lower, it has been shown that drilling holes along the radius of the discs does improve the heat transfer out of the stator and keeps the stator cooler. Previous literature as well as model predictions stating that larger rotor – stator gaps do not reduce the windage power loss has been verified.

Finally, the efficiency of the system has been determined; showing that with the reactances discussed earlier, the efficiency changes with speed. The exact source of this reactance is unknown but research will be done, and further tests will be carried out to

reveal all possible causes of this effect in the different parts of the rig. The power density of the motor has also been determined.

Future Work

Some work could be done on the test rig to improve its performance and reduce its losses. Modifications could be made to parts and new parts could be added. The saturation current could be increased by altering the rotor – stator gap sizes either by reducing the gaps in the generator or increasing the gaps in the motor. More research could be done to learn methods that could be used to reduce the total reactance in the rig, and increase the peak efficiency. With this research, new stators could be designed using different wires that have been reliably tested for their AC reactance. The variation of efficiency with speed can be eliminated by designing and installing a motor and control to rotate the generator stator, hence adjusting the phase, while the rotor is spinning. With this, the power factor can be very close to unity and the maximum possible power can be produced at all speeds.

The temperature of the stators can be made even lower by installing fins on the stator, making sure parts of the fins are embedded very close to the gaps as is shown in Fig. 90. Also, if new stators are made, the thicker outer parts could be made hollow, with some kind of cooling jacket installed inside them. For example, copper tubing with cold water running in it could be installed as the cooling method. If new magnetic discs are designed, they should be made such that larger holes can be drilled to allow for more airflow into the gaps, especially at high speeds.

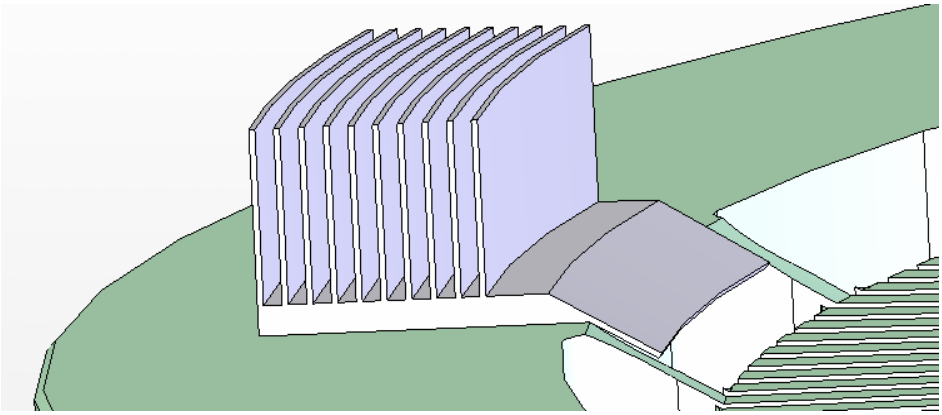

Fig. 90 Drawing of cooling fins on stator

The losses evaluated in the coast-down tests included losses from the loads exerted by the auxiliary motor. This could be improved and used to show only the losses from the test motor by designing a system to uncouple it from the auxiliary motor before the coast-down commences. This could be done by making the belt longer and installing movable idler pulleys, as shown in Fig. 91, that are controlled by an actuator.

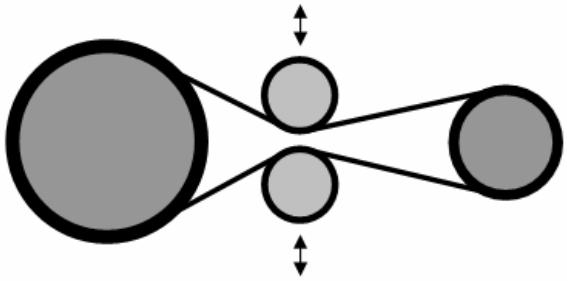

Fig. 91 Pulley system with idler pulleys

With this design, the idler pulleys could be moved immediately before coast-down commences, thus loosening the belt and uncoupling the rotor and auxiliary motor pulleys.

With further research and testing done on this test motor, results could be generally improved. With the novelty and uniqueness of the motor, when modifications

have been made and new parts with better systems as discussed earlier have been installed, the motor could be very applicable and could be used in the blade tips of aircrafts, like it was originally designed for.

Conclusion

The test motor has been designed, fabricated, built, modeled, tested and modified. The results have been analyzed and discussed. The key findings from the tests were:

- the output voltage does increase linearly with speed
- the rig and particularly the litz wire have some AC reactance that cause the current to saturate to a constant value, and cause the power to increase linearly with speed after a certain speed
- the stator heats up due to windage power losses but can be cooled by getting cold air into the rotor – stator gaps
- windage losses do not decrease significantly with an increase in the rotor – stator gaps
- the total losses from the system can be almost accurately evaluated by recording speeds and times while the motor coasts down in speed
- the efficiency changes with speed and a peak value of 82.9 % was evaluated.
- the power density of the motor is 33.1 W/lb based on the rotor weight of 497 lb and 8.8 W/lb based on the combined rotor and housing weight of 1870 lb.

The power density based on the combined weight of the rotor and the housing could be improved by reducing the weight of the housing and the efficiency could be improved by researching ways to reduce the impedance of the rig. Further research is being carried

out and additional work is being done to increase the output current and to cool the stator better.

Electric motors have been researched for a long time, and by different organizations. They can and have been used for a variety of applications from automobile wheels, to solar car drag racing. However, its use in the aircraft industry is currently not very prominent but could be a big breakthrough to end the dependence on fuels and to reduce emissive gases in the air. The test motor researched is the first of its kind. It has yielded good, educating, and interesting results that could be very useful as a starting point by future researchers, and as a reference for ongoing work in similar fields.

REFERENCES

[1] Rajashakera K., 1994, “History of Electric Vehicles in General Motors”, IEEE Transactions on Industry Applications, **30** (4), pp. 897-904.

[2] Kohout L. L., Schmitz P. C., 2003, “Fuel Cell Propulsion Systems for An All-Electric Personal Air Vehicle”, NASA/TM, Cleveland, Ohio.

[3] Masson P. J., Luongo C. A., 2005, “High Power Density Superconducting Motor for All-Electric Aircraft Propulsion”, IEEE Transactions on Applied Superconductivity, **15** (2), pp. 2226-2229.

[4] Masson P. J., Soban D. S., Upton E., Pienkos J. E., Luongo C. A., 2005, “HTS Motors in Aircraft Propulsion: Design Considerations”, IEEE Transactions on Applied Superconductivity, **15** (2), pp. 2218-2221.

[5] Ramsden V. S., Mecrouw B. C., Lovatt H. C., 1997, *Design of an In-Wheel Motor for a Solar-Powered Electric Vehicle,* EMD’97, London, UK.

[6] Brown G. V., Kascak A. F., 2005, "Fan-Tip-Drive" High-Power-Density, Permanent Magnet Electric Motor and Test Rig Designed for a Nonpolluting Aircraft Propulsion Program. http://www.grc.nasa.gov/WWW/RT/2003/5000/5930kascak.html

[7] Mills A.F., 1999, *Heat Transfer*. 2nd ed. Prentice Hall, Upper Saddle River, New Jersey, pp. 415-420.

[8] Etemad M. F., Pullen K., Besant C. B., Baines N., 1992, “Evaluation of Windage Losses for High-speed Disc Machinery”, Part A: Journal of Power and Energy, **206** (3), pp. 149-157.

[9] Tesla Turbine Pump. The Internet Glossary of Pumps. The Animated Software Company, February 2002. http://www.liu.edu/cwis/CWP/library/workshop/citinter.htm

[10] Zimmermann H., Firsching A., Dibelius G. H., Ziemann M., 1986, "Friction Losses and Flow Distribution for Rotating Disks With Shielded and Protruding Bolts", ASME Journal for Gas Turbines and Power, **108**, pp. 547-552.

[11] Skin Effect. Wikipedia, June 8, 2004. http://en.wikipedia.org/wiki/Skin_effect

[12] Amara Y., Wang J., Howe D., 2005, "Analytical Prediction of Eddy-Current Loss in Modular Tubular Permanent-Magnet Machines", IEEE Transaction on Energy Conversion, **20** (4), pp. 761-770.

VITA

Name:	Imoukhuede Tim Odion Dibua
Address:	FMC Technologies, 1803 Gears Road, Houston, TX, 77067
E-mail Address:	otdibua@hotmail.com
Education:	B.S., Mechanical Engineering, Texas A&M University, 2004
	M.S., Mechanical Engineering, Texas A&M University, 2006